RESEARCH ARTICLE

Experimental determination of forces applied by liquid water drops at high drop velocities impacting a glass plate with and without a shallow water layer using wavelet deconvolution

Y. Yu[1] · C. Hopkins[1]

Abstract

Time-dependent forces applied by 2 and 4.5 mm diameter drops of water (with velocities up to terminal velocity) impacting upon a glass plate with or without a water layer (up to 10 mm depth) have been measured using two different approaches, force transduction and wavelet deconvolution. Both approaches are in close agreement for drops falling on dry glass. However, only the wavelet approach is able to measure natural features of the splash on shallow water layers that impart forces to the plate after the initial impact. At relatively high velocities (including terminal velocity) the measured peak force from the initial impact is significantly higher than that predicted by idealised drop shape models and models from Roisman et al. and Marengo et al. Hence empirical formulae are developed for the initial time-dependent impact force from drops falling at (a) different velocities up to and including terminal velocity onto a dry glass surface, (b) terminal velocity onto dry glass or glass with a water layer and (c) different velocities below terminal velocity onto dry glass or glass with a water layer. For drops on dry glass, the empirical formulae are applicable to a glass plate or a composite layered plate with a glass surface, although they apply to other plate thicknesses and are applicable to any plate material with a similar surface roughness and wettability. The measurements also indicate that after the initial impact there can be high level forces when bubbles are entrained in the water layer.

1 Introduction

1.1 Motivation

Understanding liquid drop impacts on dry or wet surfaces is important in many different areas of engineering such as blade erosion in steam turbines, soil splash from raindrops, ink jet printing, spray coating of paper and medical applications such as drop impacts onto the eye. The surfaces of interest vary widely and can be rigid, soft, elastic, structured, non-porous or porous. For many applications, it is necessary to have knowledge of the force applied by the liquid drop upon impact to allow an assessment of erosion, damage, or the efficacy of the impact process.

For rainfall on windows and roofs in buildings, cars, trains or ships, the force from the raindrops is relatively high due to the drops travelling at terminal velocity. The raindrops excite bending waves on the structure that can generate high levels of re-radiated sound that adversely affects speech communication or other activities. Prediction of the sound and vibration resulting from the impact of raindrops requires knowledge of the time-dependent force that is applied to a structure when it is dry or covered with a shallow surface layer of water. This provides the motivation for the current study to experimentally determine the time-dependent forces that are applied by drops at high velocities.

1.2 Properties of rain

Natural rain is comprised of different size drops for which the distribution of drop sizes depends on the rainfall rate (Marshall and Palmer 1948). Light rain with a rainfall rate of 1 mm/h will rarely give rise to significant re-radiated noise problems; hence it is of more interest to consider moderate to heavy rain which typically has rainfall rates from 4 to 50 mm/h (IEC 2013). For light to heavy rain, raindrops can generally be described as spherical or ellipsoidal in shape using the concept of an equivalent sphere (Clift et al. 1978).

✉ C. Hopkins
  carl.hopkins@liverpool.ac.uk

1   Acoustics Research Unit, University of Liverpool,
    Liverpool L69 7ZN, UK

In general, a drop shape is conveniently represented by the combination of two oblate semi-spheroids (Clift et al. 1978) although 2 mm drops at terminal velocity are approximately spherical (axis ratio is ≈ 0.9; Beard et al. 2010). In temperate climates there is rarely any need to consider equivalent drop diameters larger than 5 mm because such drops will break up into smaller drops as they fall (IEC 1988). While natural rain contains a wide range of equivalent drop diameters, the structure-borne sound power it injects into a structure tends to be dominated by the fraction of larger diameter drops that apply a higher force due to their higher mass and terminal velocity (Ballagh 1990). The raindrop size distribution is typically considered to have equivalent drop diameters between 1 and 2 mm (IEC 2013); hence in this paper it is assumed that 2 mm drops represent the smallest drop diameter of interest for rain noise.

1.3 Models for the time-dependent force

Idealized drop shape models have been used to predict the time-dependent force applied to a dry, rigid surface. Petersson (1995) considered prediction models based on paraboloidal and cylindrical–hemispherical drop shapes for which comparison with measurements indicated that the former showed better agreement than the latter. Photographic observations (e.g., Mitchell et al. 2016) indicate that a cylindrical–hemispherical model could be more appropriate when the drop velocity on impact is low (i.e., ≈ 2 m/s). However, the deficiencies with this model were attributed to the assumption of constant velocity in the flow phase. Petersson's experiments appear to be the only published results that have attempted to quantify the force applied when there is a surface layer of water; unfortunately, the depth of this layer was not quantified, being described either as a 'thin' or 'thick' layer, and the drop velocity was not stated.

Suga and Tachibana (1994) used the paraboloidal model from Petersson to estimate the injected power from natural rainfall, but there was only one comparison of theory with laboratory measurements. Hopkins (2012) also used the paraboloidal drop shape model and statistical energy analysis (SEA) to predict the sound radiated by a glass plate which showed close agreement with measurements below 800 Hz and above 1.6k Hz. However, in the intermediate frequency range, there was a discrepancy that might be caused by the choice of idealized drop shape or the lack of consideration of a surface water layer on the glass.

In the models described above, there is no consideration of the spreading lamella (Rioboo et al. 2002). Roisman et al. (2002) used a spherical drop shape model to estimate the spreading and receding phenomenon for a liquid drop on a dry surface from which the time-dependent force was derived, but it was not compared with measurements. Anantharamaiah et al. (2006) later compared the calculated force from Roisman

et al. with their CFD simulations which showed agreement within 18% for a 4.9 mm diameter water drop with a velocity of 2.34 m/s (i.e., well-below terminal velocity). However, the 2002 Roisman et al. model is indicated as being incorrect by Marengo et al. (2011). Roisman et al. (2009) subsequently determined an empirical curve for dimensionless pressure at the impact point from curve fitting of numerical predictions for a spherical liquid drop on a dry surface.

1.4 Experimental determination of the time-dependent force

Previous experiments to measure the time-dependent force from liquid drops have used a variety of approaches. Nearing et al. (1986) used pressure sensors and noted that the time-dependent force and average pressure were not adequately predicted by theory based on incompressible mechanics or numerical techniques that do not account for compressional wave generation, surface tension, and viscosity. Nearing and Bradford (1987) used a pressure transducer to measure the force although the sensing area had a diameter of 6.45 mm so many drops did not fall on the sensor. Grinspan and Gnanamoorthy (2010) used PVDF film to measure the impact force applied by a low velocity water drop and an oil droplet on a solid surface. This showed that the impact force depends on the drop velocity and liquid density. Soto et al. (2014) used two different approaches to measure the force from a water drop: piezoelectric quartz and a thin glass lamella. The latter approach used mechanical equilibrium to determine the maximum force from the largest deformation of the lamella for a given impact. The literature indicates that a piezoelectric transducer can be problematic due to (a) resonances of the transducer-disc (e.g., Mitchell et al. 2016; Li et al. 2014), (b) drop impacts outside the small sensor area and (c) small sensors not being well-suited to impacts on shallow water layers; hence, an alternative approach using wavelet analysis for impacts on a relatively large plate is considered in this paper.

1.5 Aims

This paper concerns measurement of the time-dependent force applied by a liquid drop of water falling onto a sheet of glass when dry, and when covered with a still, shallow layer of surface water up to a depth of 10 mm. The main aim is to establish empirical formulae for the time-dependent force and assess whether this is more accurate than that predicted by idealized drop shape models. The force is determined using Doyle's wavelet deconvolution method (Doyle 1997) because of its robustness to noise and the ability to use a glass plate which provides a realistic surface condition that is relevant to roof glazing on cars and in buildings. The wavelet approach is validated through comparison with

measurements using a glass disc fixed to a force transducer. Experimental work uses 2 and 4.5 mm diameter drops at a range of velocities up to terminal velocity to give a wide range of validity for the empirical formulae. After the initial impact of the drop on a water layer, there exist a range of complex features (Prosperetti and Oguz 1993) which can also exert forces on the glass. The ability of the wavelet approach to quantify these forces is discussed, but the focus for the empirical formulae is on the prediction of the initial impact force.

2 Prediction models for the impact force on a dry surface

Four idealised drop shape models are used to predict the time-dependent impact force on a dry surface; these correspond to paraboloidal, cylindrical–hemispherical, spherical and ellipsoidal shapes. From Petersson (1995) the time-dependent force, $f(t)$, for a paraboloidal drop shape (Fig. 1a) is given by:

$$f(t) = \begin{cases} \rho_{\mathrm{w}} \pi r^2 v^2 \left(1 - \frac{3vt}{8r}\right) & 0 \le t \le 8r/3v \\ 0 & \text{for all other } t \end{cases}, \tag{1}$$

where r is the drop radius, ρ_{w} is the density of water, v is the drop velocity.

For a cylindrical–hemispherical drop shape (Fig. 1b) the force is given by (Petersson 1995)

$$f(t) = \begin{cases} \rho_{\mathrm{w}} \pi r^2 v^2 & 0 \le t \le \frac{2r}{3v} \\ \rho_{\mathrm{w}} \pi r^2 v^2 \left[\frac{5}{9} + \frac{4vt}{3r} - \frac{v^2 t^2}{r^2}\right] & \frac{2r}{3v} \le t \le \frac{5r}{3v} \\ 0 & \text{for all other } t \end{cases}. \tag{2}$$

Two additional drop shape models have been derived for this paper, a spherical drop shape model (Fig. 1c) giving:

$$f(t) = \begin{cases} 2\rho_{\mathrm{w}} \pi r v^3 t - \rho_{\mathrm{w}} \pi v^4 t^2 & 0 \le t \le 2r/v \\ 0 & \text{for all other } t \end{cases}, \tag{3}$$

and an ellipsoidal drop shape model (Fig. 1d) giving:

$$f(t) = \begin{cases} \rho_{\mathrm{w}} \pi v^2 \left[a^2 - \frac{a^2}{b_1^2}(b_1 - vt)^2\right] & 0 \le t \le b_1/v \\ \rho_{\mathrm{w}} \pi v^2 \left[a^2 - \frac{a^2}{b_2^2}(b_1 - vt)^2\right] & \frac{b_1}{v} \le t \le \frac{b_1 + b_2}{v} \\ 0 & \text{for all other } t \end{cases}. \tag{4}$$

The relationship between the dimensions a, b_1 and b_2 for the two oblate spheroids are (Clift et al. 1978):

$$b_1 = \frac{a}{\left[1 + 0.18(E_{\mathrm{o}} - 0.4)^{0.8}\right]\left[1 + 0.12(E_{\mathrm{o}} - 0.5)^{0.8}\right]} \tag{5}$$

$$b_2 = \frac{2a}{1 + 0.18(E_{\mathrm{o}} - 0.4)^{0.8}} - b_1, \tag{6}$$

where E_{o} is the Eötvös number which is defined as

$$E_{\mathrm{o}} = (\rho_{\mathrm{w}} - \rho_0)gD^2/\sigma, \tag{7}$$

in which g is the acceleration due to gravity, ρ_0 is the density of air, D is the drop diameter, and σ is the surface tension.

From the Roisman et al. (2009) empirical model, the dimensionless pressure at the impact point is given by

$$\bar{p}(t) = 1.7 \exp(-3.1t/(D/v)). \tag{8}$$

This dimensionless pressure can also be calculated from the Bernoulli equation as proposed by Marengo et al. (2011) where:

$$\bar{p}(t) = \frac{1}{2} + \frac{1 - 2t/(D/v)}{\pi\sqrt{t/(D/v) - (t/(D/v))^2}} \quad t/(D/v) < 0.5. \tag{9}$$
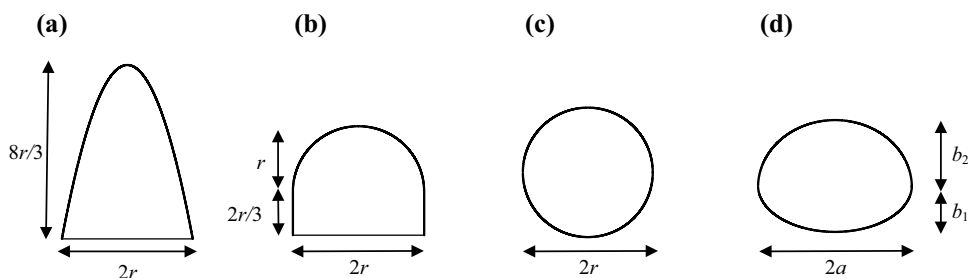
Equations (8) and (9) are compared with the idealised drop shape models by converting the dimensionless pressure to force using

$$f(t) = \bar{p}(t)\bar{a}(t)^2 \pi \rho_{\mathrm{w}} v^2 D^2, \tag{10}$$

where $\bar{a}(t)$ is the dimensionless radius of the wetted spot which can be obtained by assuming a spherical drop:

$$\bar{a}(t) \approx \sqrt{t/(D/v) - (t/(D/v))^2}. \tag{11}$$

Fig. 1 Idealised drop shapes: a paraboloidal, b cylindrical–hemispherical, c spherical, d ellipsoidal

3 Experimental set-ups

3.1 General

The experimental set-ups used for force transducer and wavelet measurements are shown in Fig. 2a, b respectively. In both set-ups the drops are released from a burette. Apart from drops travelling at terminal velocity (15 m fall height), each drop travels inside rigid plastic tubing (up to 7 m in length, 200 mm diameter); this tube shields the drop from any air movement in the laboratory. The lower end of the tubing is ≈ 0.4 m above the point of impact, and is grounded through its supporting connections. The tubing improves the repeatability of both the drop velocity on impact and the drop position on impact.

The force transducer set-up (Fig. 2a) uses a 6 mm thick glass disc fixed with cyanoacrylate glue to a 8 mm thick steel disc to ensure that the surface condition is identical in terms of wettability and roughness to the wavelet deconvolution measurements. Both disc diameters are 30 mm, which is sufficient to keep the spreading liquid within the disc boundaries after impact on a dry glass surface. The steel disc is screwed to a force transducer which is mounted on an isolated 20 kg mass to reduce the background vibration.

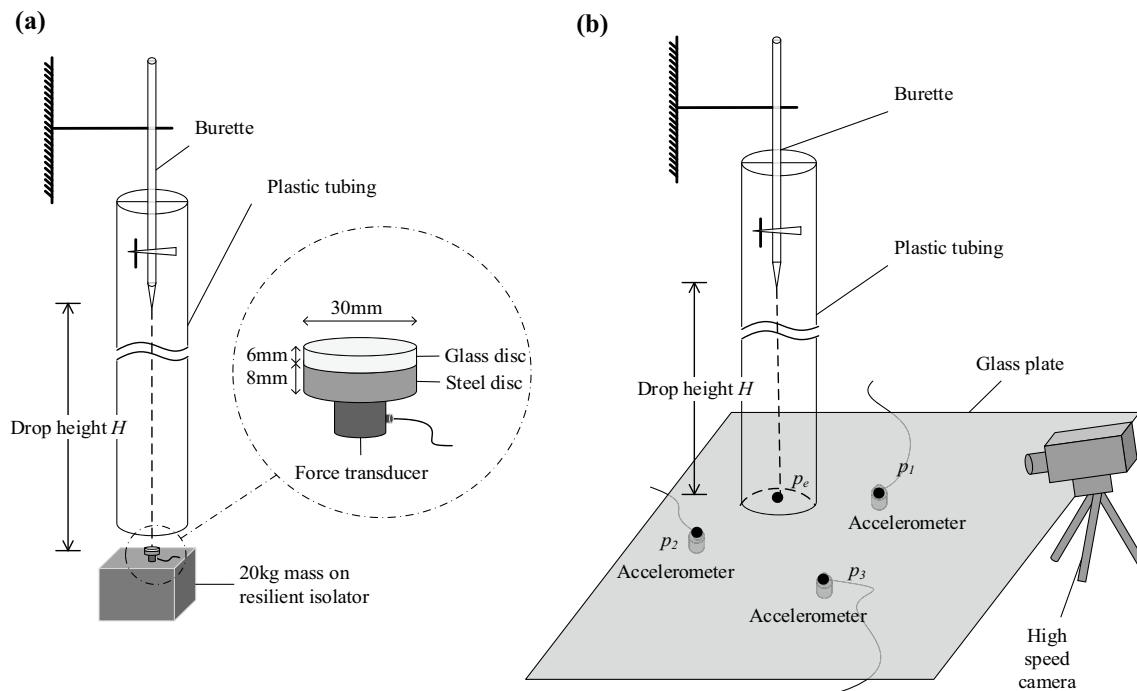In the experimental set-up for wavelet deconvolution (Fig. 2b), the drops impact upon a plate of 6 mm thick glass (1.2 m $\times 1$ m). Glass typically has an internal loss factor of 0.006; hence, to increase the overall damping of the plate (up to a loss factor of ≈ 0.05), 50 mm wide strips of 13 mm thick Sylomer SR55 are positioned on both sides of the glass around the entire perimeter with the upper layer of Sylomer compressed under a static load applied by 13 mm thick steel.

For the glass with water layers, the following water depths, d, are used: 1, 2, 4, 6, 8, and 10 mm. The variation of the water depth over the surface is estimated to be at most ± 0.5 mm. For the force transducer measurement, thin plastic tape is wrapped around the perimeter of the glass disc to contain the water on top of the disc. Before each measurement, all glassware was cleaned and dried.

Images of the impacting drop were captured using a high-speed camera (Lambda Type 70KS2B390F) at 5000 frames/s.

3.2 Drop generation

The liquid water drops are created from reverse osmosis water to remove 90–99% of most contaminants (NB use of a deionization process to provide a higher level of purity was not deemed appropriate as the aim was to assess raindrops). During all experiments the temperature was 21–25 °C, with relative humidity of 40–60%. The burette produces 4.5 mm diameter drops, to which a needle is attached to produce 2 mm diameter drops. To ensure repeatable drops

Fig. 2 Experimental set-ups: **a** force transducer-disc, **b** glass plate used for wavelet deconvolution

of approximately constant weight, Guigon et al. (2008) used relatively slow drop formation times ranging from 10 to 60 s; in the current paper, times ranging from 10 to 30 s are used. To achieve a range of drop velocities up to terminal velocity, fall heights were 0.41, 0.81, 1.63, 3.25, 6.5 and 15 m.

3.3 Drop diameter and drop velocity measurements

The drop diameter before impact is measured using two different approaches: (1) calibrating the frame dimension of a high-speed camera (Lambda Mega Speed HHC X2) to capture an image of the drop just before impact, and (2) measuring the total mass of 200 drops and calculating the diameter. The difference between the drop diameter determined using these two methods is < 0.05 mm; however, the quoted drop diameters in this paper correspond to those measured with the high-speed camera.

The drop velocity just before impact is measured using the high-speed camera with an average velocity calculated from ten drops at each fall height. The frame rate is 2000 frames/s for which the drop velocity on impact is estimated using between 10 and 20 frames up to the last frame before impact. The absolute error in the velocity is estimated to be < 8%.

3.4 Signal capture and signal processing

3.4.1 General

Force and acceleration signals are all recorded using a Brüel and Kjær PULSE analyser with a sampling rate of 131k Hz, and low-and high-frequency cut-offs of 10 and 10k Hz, respectively (although the high-frequency cut-off is extended to 100k Hz when measuring bubble entrainment). The frequency resolution is 0.5 Hz for the FFT data after zero padding in time domain and these narrow bands are used for the comparison of measured data. However, to determine and assess the empirical formulae the narrow bands are combined into one-third octave bands because (a) the smoother curves in the frequency domain are better suited to curve fitting and (b) these bands are typically used to assess human response to noise.

3.4.2 Force transducer method

The sensor used to determine the force is a piezoelectric force transducer (Brüel and Kjær Type 8200). The first structural mode of the force transducer-disc system causes ringing between 7.5k and 8.5k Hz. Hence a second-order, band-stop Butterworth filter (low- and high-frequency cut-off at 7k and 9k Hz, respectively) is used to remove the

ringing without significantly changing the measured force below 6k Hz.

3.4.3 Wavelet deconvolution

When an unknown force, $\mathbf{f}$, excites a noiseless LTI system, a matrix of transfer accelerances, $\mathbf{X}$, describes the acceleration, $\mathbf{e}$, at points on this system by a linear convolution integral. Each transfer accelerance is the ratio of complex acceleration at a specified position to the complex force applied at another specified position. The discrete time domain acceleration can be expressed as (Vaseghi 2013):

$$\mathbf{e} = \mathbf{Xf}. \tag{12}$$

Wavelet deconvolution is used to determine the time-dependent force using an approach described by Doyle (1997). Doyle's theory assumes that there is no noise; hence, the unknown force is estimated according to (Doyle 1997):

$$\mathbf{f} = \mathbf{\Phi}^{\mathrm{H}}\mathbf{f_w} = \mathbf{\Phi}^{\mathrm{H}}(\mathbf{\Psi}\mathbf{\Psi}^{\mathrm{H}})^{-1}\mathbf{\Psi}\mathbf{e}, \tag{13}$$

where superscript H is the Hermitian, $\mathbf{\Phi}$ is an $M \times N$ matrix of wavelet functions with elements $\phi_m(t_n) = \exp\left[-\left(\frac{t_n - mt_0}{\alpha}\right)^2\right]$, t_n is the nth sample in time, α is the scaling factor (which is dependent on the frequency range of analysis), m is the time shift integer, $\mathbf{f_w}$ (subscript w indicates wavelet) is a vector with dimension M to replace the original unknown vector $\mathbf{f}$ with dimension, N, and $\mathbf{\Psi}$ is defined as

$$\mathbf{\Psi} = \mathbf{\Phi}\mathbf{X}^{\mathrm{H}}, \tag{14}$$

where the elements are a matrix of functions $\psi_m(t_n) = \sum_{k=0}^{n-1} x(t_n - \tau_k)\phi_m(\tau_k)$.

In practise there will always be some unwanted noise. To consider the effect of additive noise in Eq. (12) requires the unknown force to be transformed to the wavelet domain, so it can be rewritten as:

$$\mathbf{e} = \mathbf{X}\mathbf{\Phi}^{\mathrm{H}}\mathbf{f_w} + \mathbf{n} = \mathbf{\Psi}^{\mathrm{H}}\mathbf{f_w} + \mathbf{n}, \tag{15}$$

where $\mathbf{n}$ is the noise vector.

The aim is to estimate the M-dimensional vector $\mathbf{f_w}$ from an N-dimensional observation vector, $\mathbf{e}$. Assuming that the matrix $\mathbf{\Psi}^{\mathrm{H}} = \mathbf{X}\mathbf{\Phi}^{\mathrm{H}}$ has been determined from measurements in the presence of noise, the likelihood function of the signal, $\mathbf{e}$, given the parameter vector, $\mathbf{f_w}$ is:

$$f_{\mathbf{E}|\mathbf{F_w}}(\mathbf{e}|\mathbf{f_w}) = f_{\mathbf{n}}(\mathbf{n} = \mathbf{e} - \mathbf{\Psi}^{\mathrm{H}}\mathbf{f_w}). \tag{16}$$

Assuming that $\mathbf{n}$ is random noise with a Gaussian distribution of mean, $\mathbf{\mu_n}$, and a covariance matrix, $\mathbf{\Sigma_{nn}}$, and that the parameter vector, $\mathbf{f_w}$, is also a Gaussian process with

mean, μ_{f_w}, and a covariance matrix, $\Sigma_{f_w f_w}$ then the likelihood function is:

$$f_{E|F_w}(e|f_w) = f_n(n)$$
$$= \frac{1}{(2\pi)^{\frac{N}{2}}|\Sigma_{nn}|^{\frac{1}{2}}}\exp\left[-\frac{1}{2}(e - \Psi^H f_w - \mu_n)^H \Sigma_{nn}^{-1}(e - \Psi^H f_w - \mu_n)\right]. \tag{17}$$

The Maximum Likelihood Estimate (MLE) is obtained from maximization of the log-likelihood function, $\ln[f_{E|F_w}(e|f_w)]$, with respect to f_w and is given by (Vaseghi 2013):

$$\Psi\Psi^H f_w = \Psi(e - \mu_n) \tag{18}$$

and when $\Psi\Psi^H$ is well-posed,

$$f_w = (\Psi\Psi^H)^{-1}\Psi(e - \mu_n). \tag{19}$$

The system impulse response can be measured using force hammer excitation with accelerometers at a number of response positions. The unknown force applied by the real impact can then be related to the impact force, $\bar{f}$, applied by the force hammer, and the associated acceleration signal, $\bar{e}$ (Nearing et al. 1986) by

$$e * \bar{f} = \bar{e} * f. \tag{20}$$

Equations (18) or (19) can then be solved by substituting $e * \bar{f}$ for e and $\bar{e}$ for X. If $\mu_n = 0$, then the noise is defined as white Gaussian noise and Eq. (19) is the same as Eq. (13); hence the wavelet approach can be considered as being robust against this form of noise. However, depending on the experimental conditions, X can be sparse causing matrix $\Psi\Psi^H$ to be ill-conditioned which can lead to instability in the solution of Eq. (19). To overcome this problem, Eq. (18) can be solved using the LSQR algorithm (Paige and Saunders 1982) to give f_w.

In the experiment, the matrix of transfer accelerances, X, is determined by applying an impact force at the excitation position, p_e, using a force hammer with a 3 mm diameter steel tip (Brüel and Kjær Type 8203). The acceleration at sensing positions, p_1, p_2 and p_3 was measured using three accelerometers (Brüel and Kjær Type 4375) fixed with cyanoacrylate glue to the underside of the glass plate at randomly located positions. Ten hits were averaged to give each transfer accelerance value.

When the drop impacts upon the plate, Eqs. (13) and (19) are used to calculate the time-dependent forces from the acceleration measured at the same three accelerometer positions that are used to determine the matrix X. Impacts from eight drops are averaged in the time domain. Note that for the glass with a surface water layer, the underside of the glass was used to apply the force and fix the accelerometer.

4 Results and analysis

4.1 Drop velocity on impact

The drop velocity results determined for different fall heights using the high-speed camera are shown in Table 1. These can be compared with the empirical equation from Range and Feuillebois (1998):

$$v = \sqrt{\frac{g(1 - \exp(-2AH))}{A}}, \tag{21}$$

where

$$A = \frac{3c_f\rho_0}{8\rho_w r}, \tag{22}$$

in which c_f is the friction coefficient, H is the fall height, and r is the equivalent radius of the drop, which can be calculated using (Roux and Cooper-White 2004):

$$r = (r_h^2 r_v)^{1/3}, \tag{23}$$

where r_h and r_v are the horizontal and vertical radii of the drop respectively.

The friction coefficient is given by Serafini's equation (Fuchs 1964) and is a function of the Reynolds number but this equation is only valid over a limited range where

Table 1 Drop velocity on impact estimated from high-speed camera measurements for the different fall heights

Drop diameter (mm)		Fall height (m)					
		0.41	0.81	1.63	3.25	6.5	15
2	Mean velocity (m/s)	2.57	3.49	4.62	5.71	This fall height was not used	6.55
	Standard deviation (m/s)	0	0.04	0.18	0.18		0.15
4.5	Mean velocity (m/s)	2.69	3.77	5.18	6.73	8.20	9.17
	Standard deviation (m/s)	0.01	0.01	0.05	0.07	0.15	0.25

$Re < 1000$; hence for a range of fall heights from 0.25 to 1.75 m, Range and Feuillebois (1998) adjusted the friction coefficient to fit their measurements with 3.6 mm diameter drops which resulted in $c_f = 0.796$. For the range of fall heights in the present experiment, $5140 < Re < 13{,}100$ for 2 mm drops and $12{,}165 < Re < 41{,}265$ for 4.5 mm drops where the Reynolds number, Re, is given by

$$Re = \frac{\rho_w v D}{\mu}, \tag{24}$$

where μ is the viscosity of water, and the Weber number, We, is given by

$$We = \frac{\rho_w v^2 D}{\sigma}. \tag{25}$$

The mean-square error was minimised giving $c_f = 0.533$ for which the empirical equation is compared with measured data in Fig. 3. Additional measurements were carried out without a tube around the 4.5 mm drops with fall heights between 0.42 and 5.5 m; these confirmed the use of $c_f = 0.533$ and that the presence of the tube has negligible effect on the drop velocity. The reason for the difference compared with c_f from Range and Feuillebois is likely to be due to the wider range of fall heights and the two different drop sizes considered in the current experiment.

4.2 Impact force from water drops on dry glass

4.2.1 Experimental results

For 2 and 4.5 mm drops, Fig. 4 shows the results from wavelet and force transducer measurements for a dry glass surface

in terms of the time-dependent force and the corresponding energy spectral density (ESD) in the frequency domain. Note that force transducer measurements were not possible at terminal velocity due to the variability in the position of the drop impact after travelling a height of 15 m. This was not problematic for the wavelet approach because the impact position on the glass could be marked after the drop had impacted to allow subsequent accelerance measurements with the force hammer.

In the time domain, the peak force increases and the pulse width decreases with increasing drop velocity. In the frequency domain, the differences between wavelet and force transducer measurements are < 1.6 dB except at the lowest velocity where the former is up to 3.7 dB lower than the latter at high frequencies. These small differences are likely to be caused by the modal response of the force transducer-disc system even though a band-stop filter was used to minimise any effect. The fact that both measurements show close agreement means that the wavelet approach can be considered to be reliable.

4.2.2 Empirical formulae

In Sect. 4.2.1 the wavelet approach was validated by the agreement with the force transducer, however, because the transducer-disc system can be adversely affected by ringing from the first structural mode, only the wavelet approach is used to determine the empirical formulae.

Based on the force profiles, the following empirical formula is identified for the time-dependent force which is dependent on three parameters, C, α, β:

$$f(t) = f(t; C, \alpha, \beta) = C \exp[-(\ln(1000t) + \alpha)^2/\beta^2]. \tag{26}$$
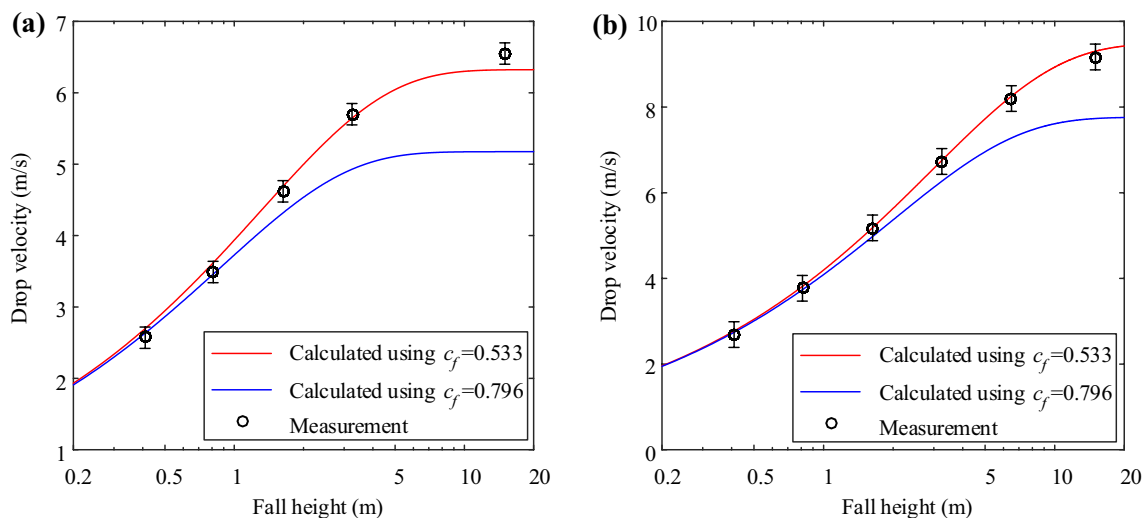
Fig. 3 Comparison of measured (average with 95% confidence intervals) and calculated drop velocity at different fall heights: **a** 2 mm drops, **b** 4.5 mm drops
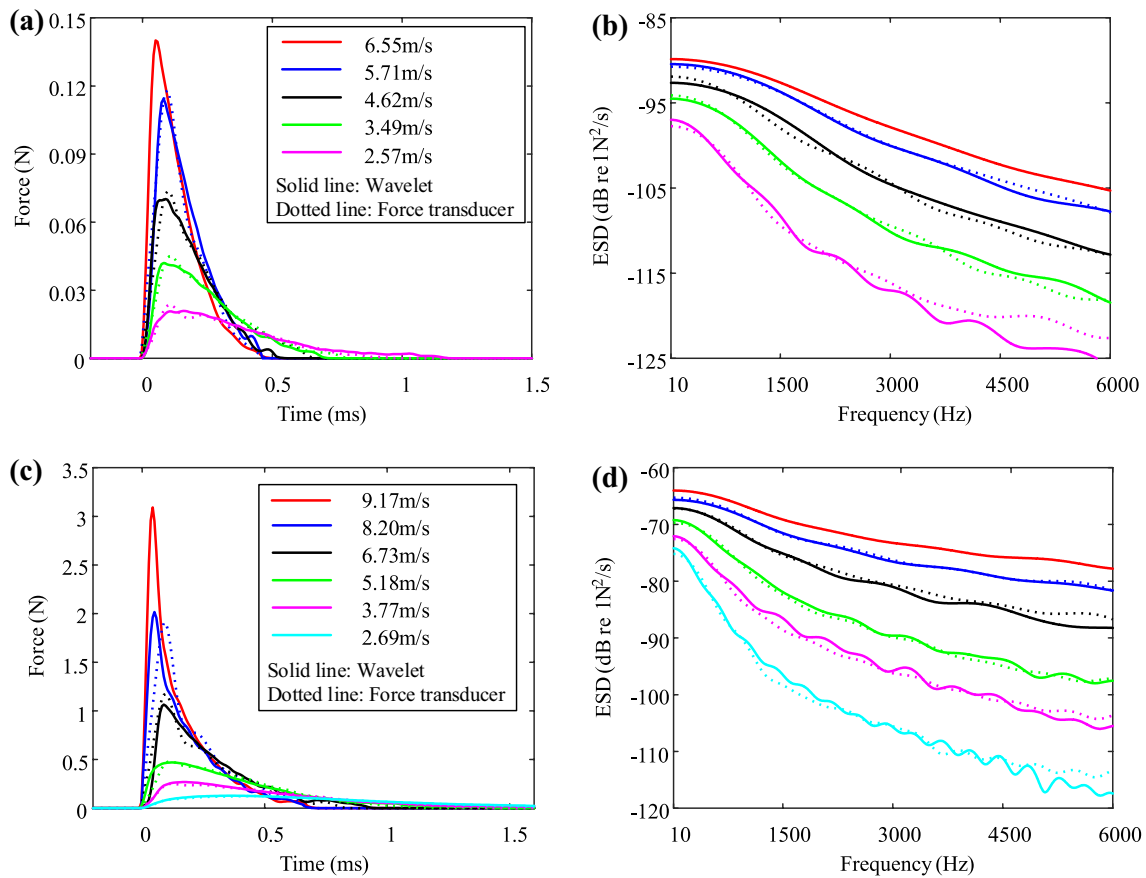
Fig. 4 Measured time-dependent force and ESD determined using the wavelet approach and the force transducer with different drop velocities impacting a dry glass surface: **a, b** 2 mm drops, **c, d** 4.5 mm drops

The absolute error between this formula and the wavelet approach is minimized using the l2-norm to give optimized parameters C, α, β in the frequency domain to cover all one-third octave bands between 12.5 and 5k Hz using:

$$\underset{C,\,\alpha,\beta}{\text{argmin}} \,\, \left\| f(\text{frequency};\, C,\,\alpha,\beta) - f_{\text{wavelet}}(\text{frequency}) \right\|_2 . \quad (27)$$

A least-squares approach is then used to give a linear relationship between the parameters $\ln(C)$, α, β and drop velocity, v, where

$$\ln(C) = va_C + b_C \quad (28)$$

$$\alpha = va_\alpha + b_\alpha \quad (29)$$

$$\beta = va_\beta + b_\beta. \quad (30)$$

4.2.3 Comparison of measurements with empirical formulae and idealized drop shape models

For 2 and 4.5 mm drops, Fig. 5 shows a time domain comparison of the measured forces (Fig. 5a), empirical formulae (Fig. 5b), idealized drop shape models (Fig. 5c) and the

models from Roisman et al. and Marengo et al. (Fig. 5d). To facilitate the comparison of the results, dimensionless force, $f(t)/(\rho_w v^2 D^2)$, and dimensionless time, $t/(D/v)$, are used as described by Zhang et al. (2017). In the frequency domain the difference between the measured one-third octave band ESD and the empirical formulae, idealized drop shape models and the model from Roisman et al. and Marengo et al. are shown in Fig. 6.

The empirical formula for the time-dependent force is given by Eq. (26) where $C = \exp(0.4507v - 4.7951)$, $\alpha = 0.1848v + 1.3576$, $\beta = -0.0447v + 1.2157$ for 2 mm drops with drop velocities between 2.57 and 6.55 m/s, and $C = \exp(0.449v - 3.0538)$, $\alpha = 0.3386v + 0.2325$, $\beta = 0.0417v + 1.1023$ for 4.5 mm drops with drop velocities between 2.69 and 9.17 m/s. In the time domain there is close agreement between measurements and the empirical formula. In the frequency domain, the difference between measurements and the empirical formula is typically < 2 dB for 2 and 4.5 mm drops, with the larger differences occurring above 800 Hz.

Zhang et al. (2017) showed that dimensionless force and time resulted in a universal curve for the time-dependent
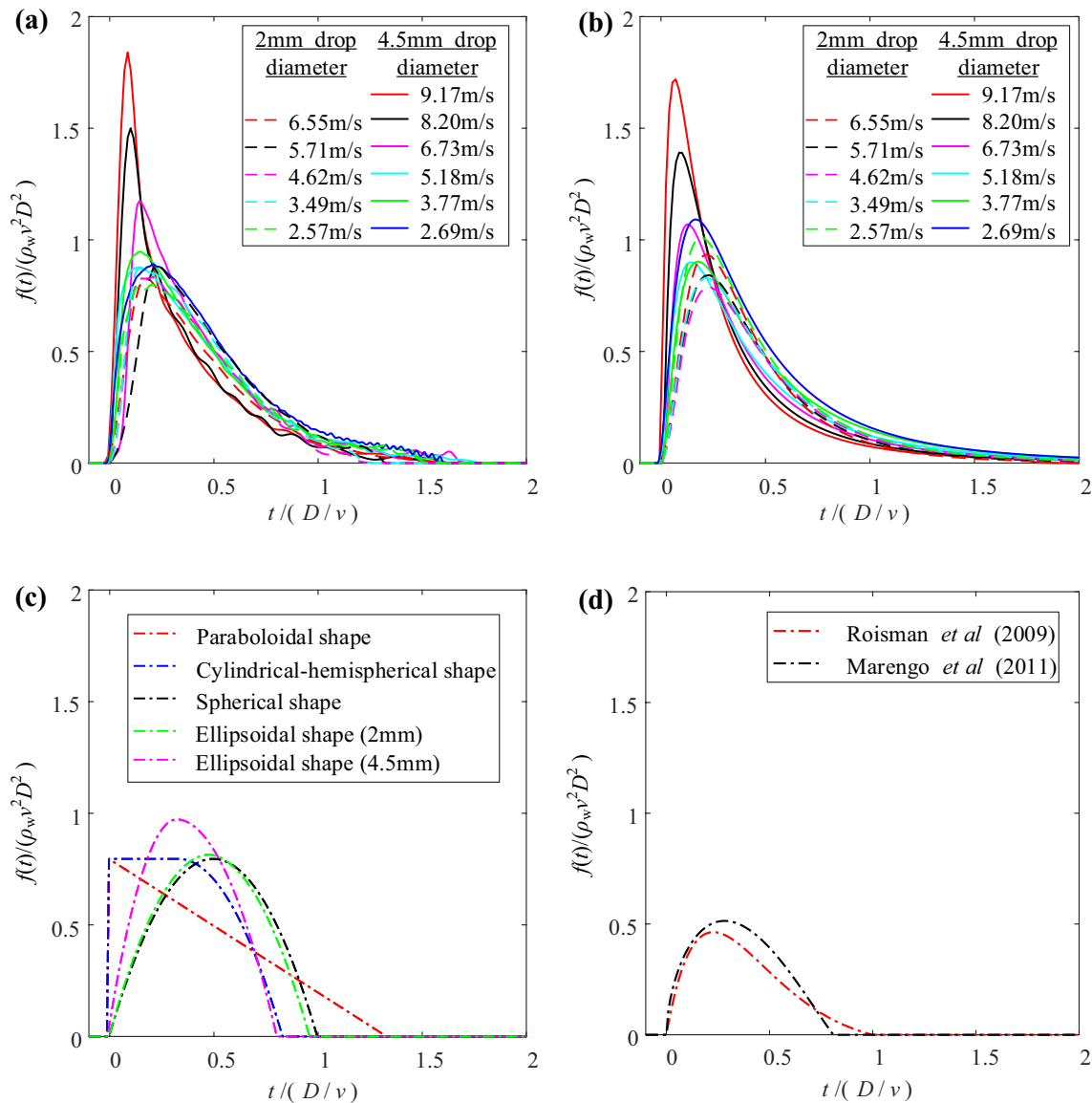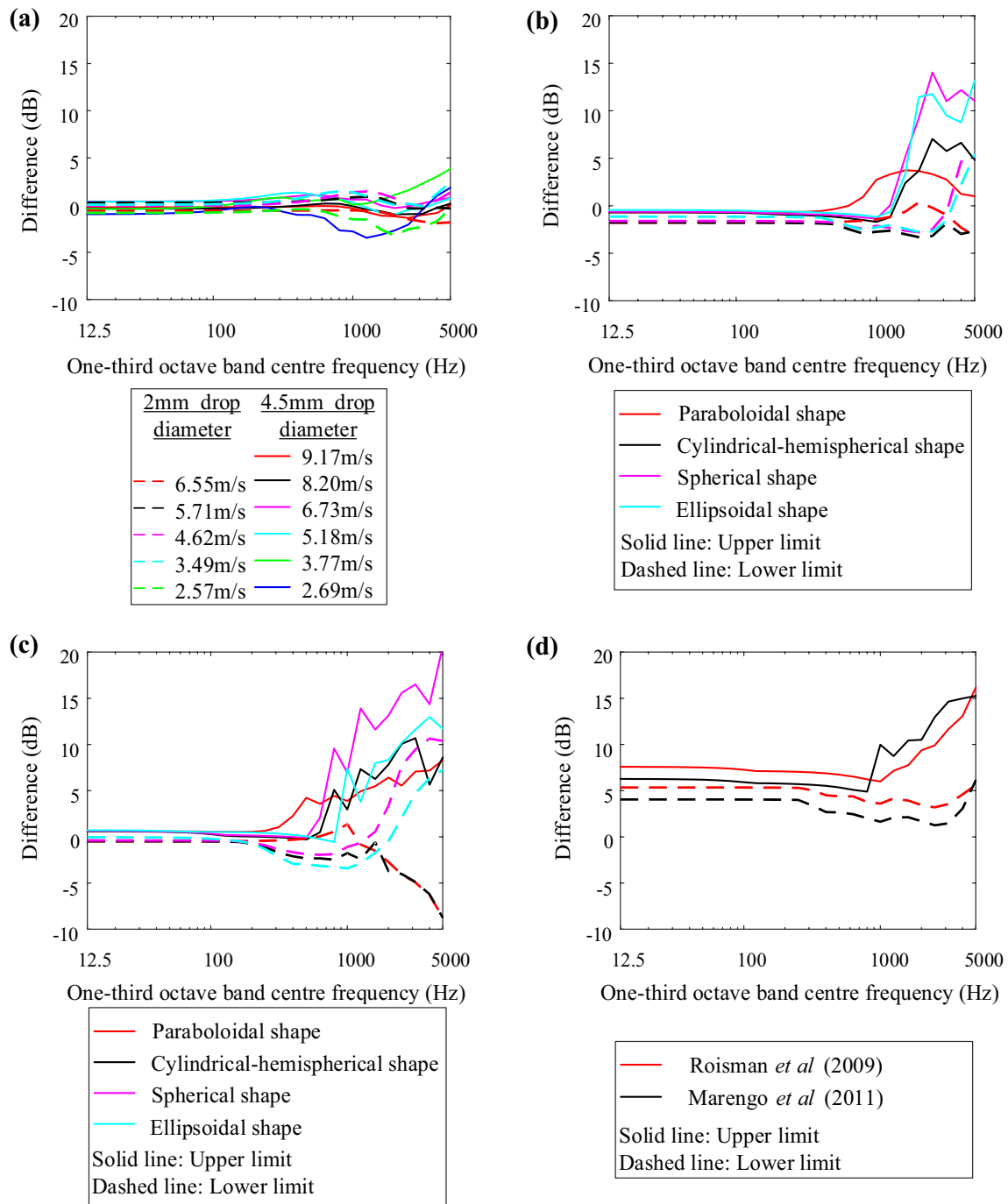
Fig. 5 Comparison of dimensionless force between measurements using the wavelet approach and different models for 2 and 4.5 mm drops with the different drop velocities impacting a dry glass surface **a** wavelet measurement, **b** empirical formulae, **c** idealized drop shape model, **d** Roisman et al. (2009) and Marengo et al. (2011) models

force when $Re > 230$ (described as an 'inertia-dominated zone' for the impact force). However, they used low drop velocities between 1.36 and 2.99 m/s (water drop diameters between 2.7 and 3.53 mm) whilst the current paper considers higher drop velocities. The results in Fig. 5a indicate that the concept of a universal curve is reasonable for all the 2 mm drops up to terminal velocity, but only up to a drop velocity of 5.18 m/s for 4.5 mm drops. For 4.5 mm drops it is clearly seen that at velocities up to and including terminal velocity (6.73, 8.20, 9.17 m/s) the dimensionless force differs significantly from the other curves. This might be caused by the flattened underside of the drop which occurs at high velocities, and would be a topic for further

research. In the frequency domain, Fig. 6a shows that the absolute difference between the wavelet measurements and the empirical formula is < 1 dB between 12.5 and 250 Hz, and < 4 dB between 315 and 5k Hz.

The idealised drop shape models tend to show less agreement with the measured force than the empirical formulae at high frequencies. In the time domain, the force increases rapidly when the water drop hits the surface of the glass, then decreases as the liquid begins to spread outward. The initial rapid rise in the force is approximated by the paraboloidal, cylindrical–hemispherical, and ellipsoidal drop shape models. However, the measured peak force for 4.5 mm drops is significantly higher than all the drop shape models with

(a)

(b)

2mm drop diameter	4.5mm drop diameter
	9.17m/s
— — 6.55m/s	— — 8.20m/s
— — 5.71m/s	— — 6.73m/s
— — 4.62m/s	— — 5.18m/s
— — 3.49m/s	— — 3.77m/s
— — 2.57m/s	— — 2.69m/s

— Paraboloidal shape
— Cylindrical-hemispherical shape
— Spherical shape
— Ellipsoidal shape
Solid line: Upper limit
Dashed line: Lower limit

(c)

(d)

— Paraboloidal shape
— Cylindrical-hemispherical shape
— Spherical shape
— Ellipsoidal shape
Solid line: Upper limit
Dashed line: Lower limit

— Roisman *et al* (2009)
— Marengo *et al* (2011)
Solid line: Upper limit
Dashed line: Lower limit

Fig. 6 Difference in the ESD (one-third octave bands) between **a** the wavelet measurement and the empirical formula for different drop velocities, **b** the wavelet measurement and idealised drop shape models for 2 mm drops in terms of the upper and lower limit from different drop velocities, **c** the wavelet measurement and idealised drop shape models for 4.5 mm drops in terms of the upper and lower limit from different drop velocities, and **d** the wavelet measurement and Roisman et al. (2009) and Marengo et al. (2011) models in terms of the upper and lower limit from different drop velocities for the 2 and 4.5 mm drops

the three highest drop velocities (9.17, 8.20 and 6.73 m/s) although it is a reasonable estimate for lower drop velocities (5.18, 3.77 and 2.69 m/s). For 2 mm drops the measured peak force is reasonably estimated by the models for the four highest drop velocities (6.55, 5.71, 4.62, 3.49 m/s) but not

for the lowest drop velocity (2.57 m/s). Note that these seemingly large errors in the time domain tend to be relatively insignificant (i.e., within ± 2 dB) in the frequency domain at low-frequencies (i.e., below 200 Hz)—see Fig. 6b, c.

The models from Roisman et al. and Marengo et al. underestimate the measured peak force in the time domain at all velocities (see Fig. 5d) which, in the frequency domain, equates to an underestimate of ≈ 5 dB below 500 Hz. Note that these errors are significantly larger than those associated with the idealised drop shape models in this frequency range which were ± 1 dB. Above 1k Hz the agreement of the models from Roisman et al. and Marengo et al. with measurements is no better than the idealised drop shape models because none of the models provide a close representation of the time-dependent force.

The motivation to develop empirical formulae stems from the fact that none of the models are able to reproduce the measured spectrum over the entire frequency range from 12.5 to 5k Hz within a few decibels; only the empirical formulae are able to do this.

## 4.3 Impact force from water drops on a shallow water layer

4.3.1 Analysis of the drop impact

With the wavelet approach there is no ambiguity about the position on the glass at which the force is applied by the impacting drop. In contrast, a drop impact on a shallow layer of water is more complex. For an impact on deep water (> 25 mm) with a sufficiently high drop velocity, the general features are the formation of a crater with a raised crown-like perimeter, followed by closure of the crater with a rising jet (often called the 'Rayleigh' or 'Worthington' jet) emanating from the centre of the aforementioned crater. A drop (or drops) may then detach from the top of the jet (Leighton 1994; Hobbs and Osheroff 1967). As with the dry surface, the position of the initial impact is well-defined, but the forces applied after the initial impact are not all applied at the same position. Hobbs and Osheroff (1967) note that for water depths < 5 mm, the crown is more unstable than with impacts on deep liquid. Any drops that detach from the crown tend to fall back onto the water layer near the rim of the crater (at its widest point) rather than at the point of initial impact. Note that no drops detach from the jet for depths < 3 mm (Hobbs and Osheroff 1967). Experimental work by Macklin and Hobbs (1969) shows that the crater has a maximum depth of up to ≈ 3 drop diameters; hence for shallow water the crater depth is affected by the presence of the rigid plate which supports the water layer, and this flattens the bottom of the crater. When the depth of the water layer is approximately equal to two drop diameters, the jet height and the number of detached drops reaches a maximum (Hobbs and Osheroff 1967; Macklin and Hobbs 1969). When the depth is similar to the drop diameter, the jet only reaches a very low height with no detaching drops (Hobbs and Osheroff 1967). At low drop velocities, the

impacting drop can coalesce with the water layer without making a splash, and without forming a jet, but making a vortex ring (Rodriguez and Mesler 1985). For a drop impact on deep water, a 2 mm drop would be expected to coalesce with drop velocities < 1.4 m/s and 4.5 mm drops with velocities < 0.8 m/s (Rodriguez and Mesler 1985). After the crater has reached its maximum diameter, capillary waves propagate outwards over the water layer and these can be expected to exert low-level forces over a wide area. To illustrate the various phenomena that occur with different water layers and drop velocity, high-speed camera images are now analysed alongside the forces measured using the wavelet approach.

For the 2 and 4.5 mm drops shown in Figs. 7 and 8, respectively, there are distinct features relating to the splash that occur with relatively high drop velocities (NB time is shown in milliseconds after the impact.). During the formation of the raised crown-like perimeter after the initial impact, a negative force occurs as the water moves upwards, and drops detach from the tines around the perimeter of the crown (see Fig. 7). The crown diameters are ≈ 15 and ≈ 31 mm for the 2 and 4.5 mm drops, respectively. Between 15 and 40 ms when the crater is formed, there is a slight peak in the force that occurs at different times depending on the depth of the water layer. Another feature occurs with the 4.5 mm drop that has a drop velocity of 8.2 m/s. For a 1 mm water depth, Fig. 8b shows a large bubble starting to form although it never makes a complete hemisphere. However, for depths between 2 and 10 mm, a large hemispherical bubble is formed above the crater with a diameter between 40 and 50 mm; an example is shown in Fig. 8c for a 2 mm layer (NB The images are very similar for water depths > 2 mm). These large bubbles tend to rupture after 180 ms; hence whilst this is an interesting feature relating to a single drop, these bubbles are less likely to form during real rainfall due to motion of the water layer from other nearby drop impacts, and other drops falling into and breaking the surface of the bubble.

For a 2 mm drop with a relatively low velocity of 2.57 m/s, the impacting drop coalesces without a splash. The measured forces are shown in Fig. 9a, b for different water layer depths depending on whether there are bubbles that are regularly entrained in the water layer (Pumphrey and Elmore 1990). Time is shown in terms of the number of milliseconds after the impact. In the centre of the crater a hemispherical dome is produced for 1 and 2 mm water layer depths, whereas a short jet is produced for 4, 6, 8 and 10 mm depths although no drops detach from these jets. For 2 mm drops falling on 6, 8 and 10 mm water layers, bubbles are regularly entrained underneath the surface which are pinched off from the bottom of the crater. For lower depths, the water layer is not deep enough to allow complete formation of a crater, so bubbles are not entrained at the bottom of the crater. As shown in Fig. 9b, the oscillating bubble acts as an exponentially decaying high-frequency sinusoid that can
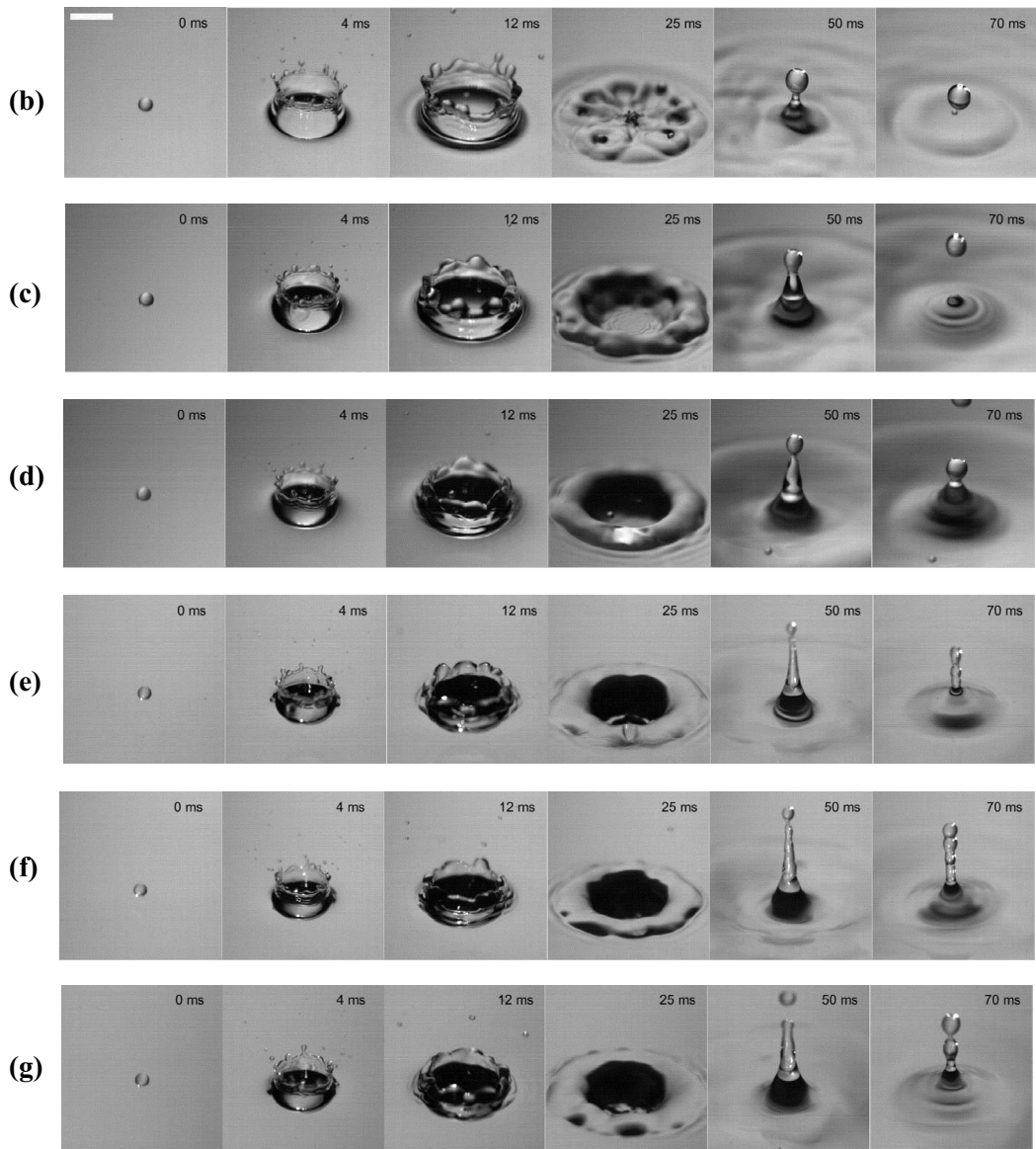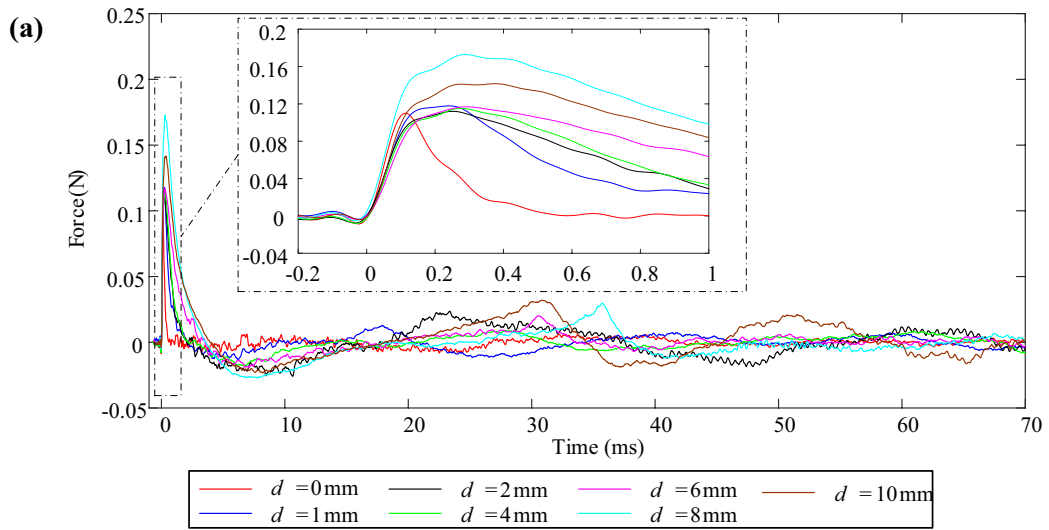
◀**Fig. 7** 2 mm drop impacting a water layer on glass with a drop velocity of 5.71 m/s. **a** Force measurements using the wavelet approach with a dry glass surface ($d = 0$ mm) and different water layer depths on the glass ranging from $d = 1$ to 10 mm (average of ten drops). High-speed camera images of a single example of a 2 mm drop impact on a water layer depth of **b** 1 mm, **c** 2 mm, **d** 4 mm, **e** 6 mm, **f** 8 mm, **g** 10 mm. Image scale bar is 6 mm long

produce significantly higher forces than the initial impact. The importance of the force applied by the oscillating bubble compared to the initial impact is assessed by windowing and zero padding (a) the initial impact, and (b) the transient associated with the oscillating bubble. This gives the ESD for the initial impact and the bubble as shown in Fig. 10. Below 200 Hz the force from the initial impact tends to be at least 9, 7 and 20 dB higher than the bubble-induced force (although this might also include low-frequency energy generated by propagating capillary waves during the transient from the bubble) for the 6, 8 and 10 mm water layers respectively. However, above 700 Hz the bubble-induced force tends to become significantly higher than that from the initial impact with high peak levels at 6.5k, 8.3k and 18.8k Hz corresponding to the bubbles generated for the 6, 8 and 10 mm water layers respectively. The frequencies, acoustic pressure and the directivity of sound radiation generated by these drops depends on the bubble size and their proximity to the surface of the water and the glass (Leighton 1994).

4.3.2 Discussion on the validity of the wavelet approach for forces applied after the initial impact

For the initial impact the force transducer and wavelet approach give similar results (which will shortly be confirmed in Sect. 4.3.3). After the initial impact it is evident that trying to contain a shallow water layer over the small area of the force transducer will introduce errors in the force that is measured during the formation of the crown up to the point that any rebounding drops from the jet return to make impact. This partly occurs because the diameter of the glass disc on the force transducer is only 30 mm, which is similar to the largest diameter of the crown or crater. Additionally, the water that is displaced is constrained, and capillary waves are not able to propagate freely away from the impact zone as they are reflected from the tape around the perimeter which is used to contain the water layer above the force transducer. In fact, sometimes water spills over the edge of the tape. This provides reasons to assess the validity of the wavelet approach after the initial impact on the basis that the approach using a force transducer is suboptimal.

The wavelet approach requires measured transfer accelerances with point excitation at the same position as the drop impact. These measurements used a force hammer with a 3 mm diameter tip, which is approximately midway between the 2 and 4.5 mm drop diameters. Hence the

acceleration measurements are considered valid for the initial impact force because the excited areas are very similar. However, the forces that occur after the initial impact are not all applied at the same position. The features that occur after the initial impact such as the formation of the crater apply forces over the perimeter of a circle with a diameter up to 7 mm, whereas the crown or vortex ring would apply forces over the perimeter of a circle with diameters between 15 and 31 mm. The jet emanates from a point that is close to the drop impact position; hence any forces associated with it should be reasonably estimated with point excitation. Some, but not all of the rebounding drops emanating from this jet will fall within the maximum crater diameter.

To make an assessment of the potential error in the forces applied after the initial impact it is assumed that in-phase forces are applied around the perimeter of a circle. Assuming an infinite plate, the driving-point acceleration with a distance, R_0, between the point at which the acceleration is measured and the excitation position can be calculated for in-phase forces around the perimeter of a circle with radius, r_c, and for point excitation. The ratio of these two accelerances is given by

$$\frac{\int_0^{2\pi} H_0^{(1)}\big(k_B R(\theta)\big) - H_0^{(1)}\big(i k_B R(\theta)\big)\mathrm{d}\theta}{2\pi\left[H_0^{(1)}\big(k_B R_0\big) - H_0^{(1)}\big(i k_B R_0\big)\right]}, \tag{31}$$

where k_B is the wavenumber for bending waves on the plate, $H_0^{(1)}$ represents the Hankel function of the first kind and the radial distance, $R(\theta)$ is

$$R(\theta) = \sqrt{(R_0 + r_c \cos\theta)^2 + r_c^2 \sin^2\theta}. \tag{32}$$

Results from Eq. (31) are shown in Fig. 11 that can be interpreted in the light of expected measurement errors. For the magnitude, it is reasonable to assume that the maximum measurement uncertainty in narrow band acceleration is 1 dB and that for the phase the variation between different accelerometers is at most 0.4° (Hopkins 2012). On this basis, an error of 1 dB in the acceleration would give an error in the impact force of ≈ 1 dB below 6k Hz. For this reason, it is concluded that after the initial impact the wavelet approach can still be used to estimate the forces (within 1 dB) that are applied by the crater, crown, jet, vortex ring, or oscillating bubbles. However, low-level forces applied by capillary waves propagating away from the crater will not be correctly estimated by the wavelet approach. Rebounding drops can fall at many different positions on the plate and, therefore, it is difficult to assess the accuracy for these forces. For rebounding drops the forces tend to be negligible in comparison with the initial impact and the oscillating bubble, but this may not always apply to the capillary waves. For this reason, the focus in Sect. 4.3.3 will be on comparing force transducer and wavelet approaches for the initial impact on
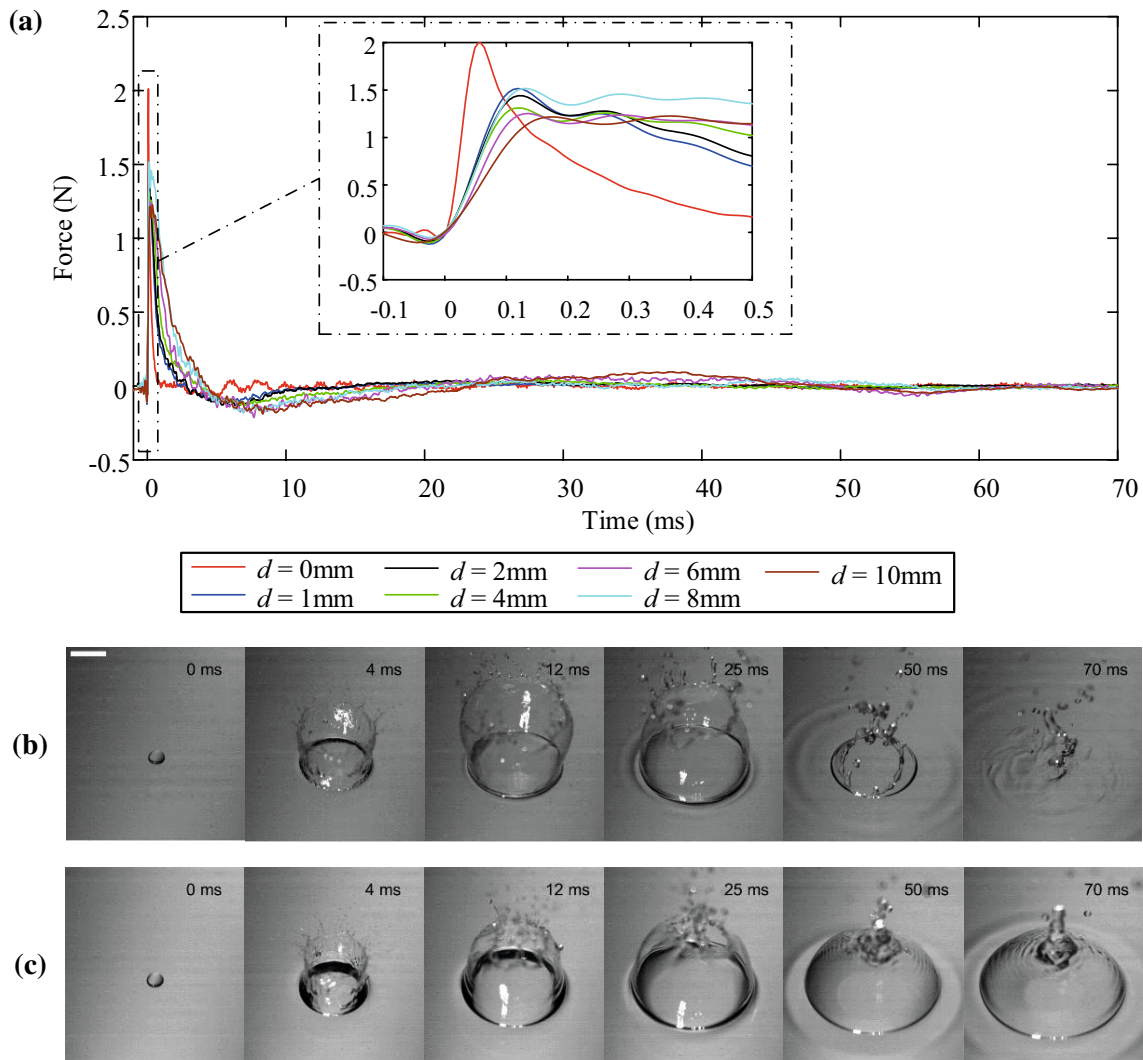
Fig. 8 4.5 mm drop impacting a water layer on glass with a drop velocity of 8.2 m/s. **a** Force measurements using the wavelet approach with different water layer depths on the glass ranging from different depths of water layer and then developing an empirical formula for the initial impact based on measurements using the wavelet approach in Sect. 4.4.

$d = 1$ to 10 mm (average of ten drops). High-speed camera images of a single example of a 4.5 mm drop impact on a water layer depth of **b** 1 mm and **c** 2 mm. Image scale bar is 10 mm long

4.3.3 Comparison of initial impact forces

Figures 12 and 13 allow comparison of the initial impact forces determined using the force transducer and wavelet approach with and without a water layer for 2 and 4.5 mm drops, respectively. This is carried out by zero padding the time signal after the initial impact. Note that for terminal velocity, there is significant variation in the drop impact position which prevents use of the force transducer-disc due to too many drops 'missing the target'; however, the wavelet approach can be used because the excitation point can be identified for each impact. With a water layer, there are differences between the force transducer and wavelet approach in terms of the peak force and pulse width in the time domain, but these only result in differences < 3 dB between 10 and 2k Hz in the frequency domain. The differences between the force transducer and wavelet approach are more apparent with deeper water depths. Considering the errors due to the modal response of the force transducer-disc system and the effect of artificially constraining a water layer on the 30 mm disc, the wavelet approach is considered to be more accurate and is the only one discussed in the remainder of this section.

Compared with dry glass, water drops impacting the various water layers apply higher forces below 500 Hz. For drops at terminal velocity, just a 1 mm water layer increases the force by ≈ 7 dB for 2 mm drops and ≈ 5 dB for 4.5 mm drops; the general trend is that as the water layer becomes
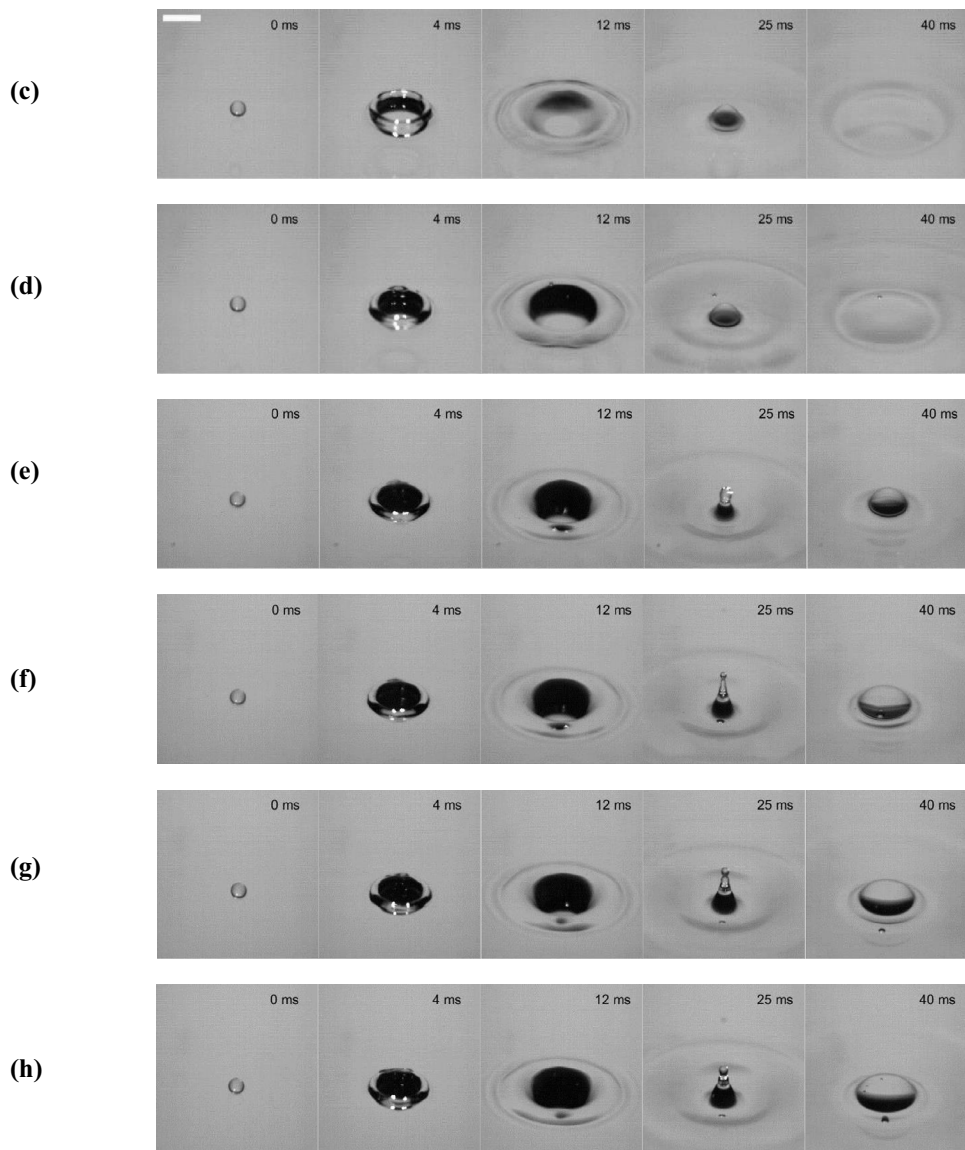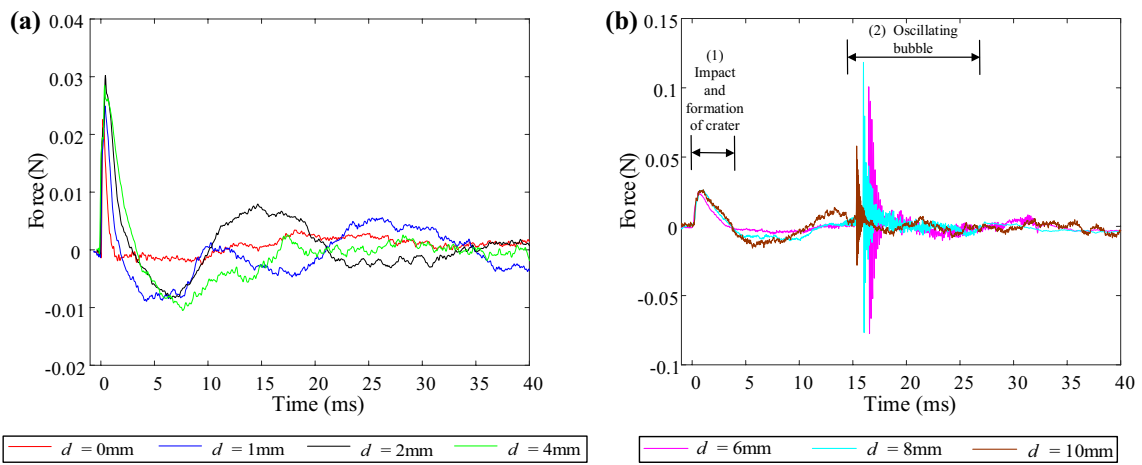
Fig. 9 2 mm drop impacting a water layer on glass with a drop velocity of 2.57 m/s. Force measurements using the wavelet approach **a** with a dry glass surface ($d=0$ mm) and water layer depths on the glass of 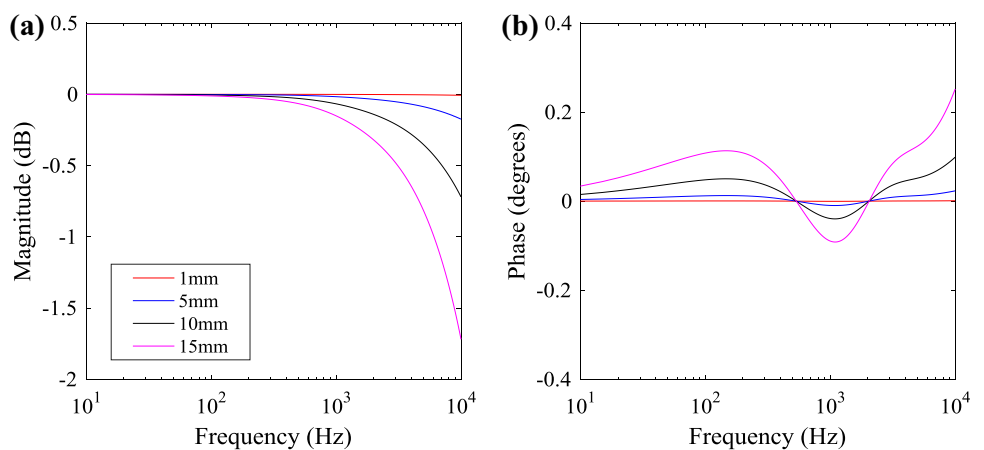$d=1$, 2 and 4 mm (average of ten drops) and **b** with water layer depths on the glass of $d=6$, 8 and 10 mm (average of ten drops). High-speed camera images of a single example of a 2 mm drop impact on a water layer depth of **c** 1 mm, **d** 2 mm, **e** 4 mm, **f** 6 mm, **g** 8 mm, **h** 10 mm. Image scale bar is 5 mm long
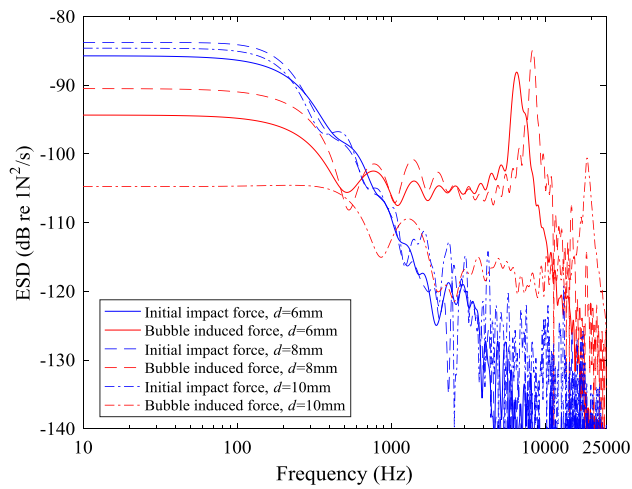
Fig. 10 Comparison between the ESD of the initial impact force and the bubble-induced force: 2 mm drop with a drop velocity of 2.57 m/s impacting onto a 6 mm water layer (average value from 10 drops), 8 mm water layer (average value from 10 drops), and 10 mm water layer (one drop)

Fig. 12 Measurements of initial impact force from 2 mm drops: ▶ **a** time-dependent force and **b** ESD with different drop velocities impacting the dry glass surface ($d = 0$ mm) and different water layer depths on the glass from $d = 1$ to 10 mm. Measurements use the wavelet approach (solid line) and force transducer (dotted line)

forces above 2k Hz. However, this change is not as significant as the increase that is observed at low-frequencies. This has practical implications for noise control from rain on the roof in buildings because roofs and roof glazing will have a surface water layer during the rainfall period, albeit a moving layer of water down a sloped surface.

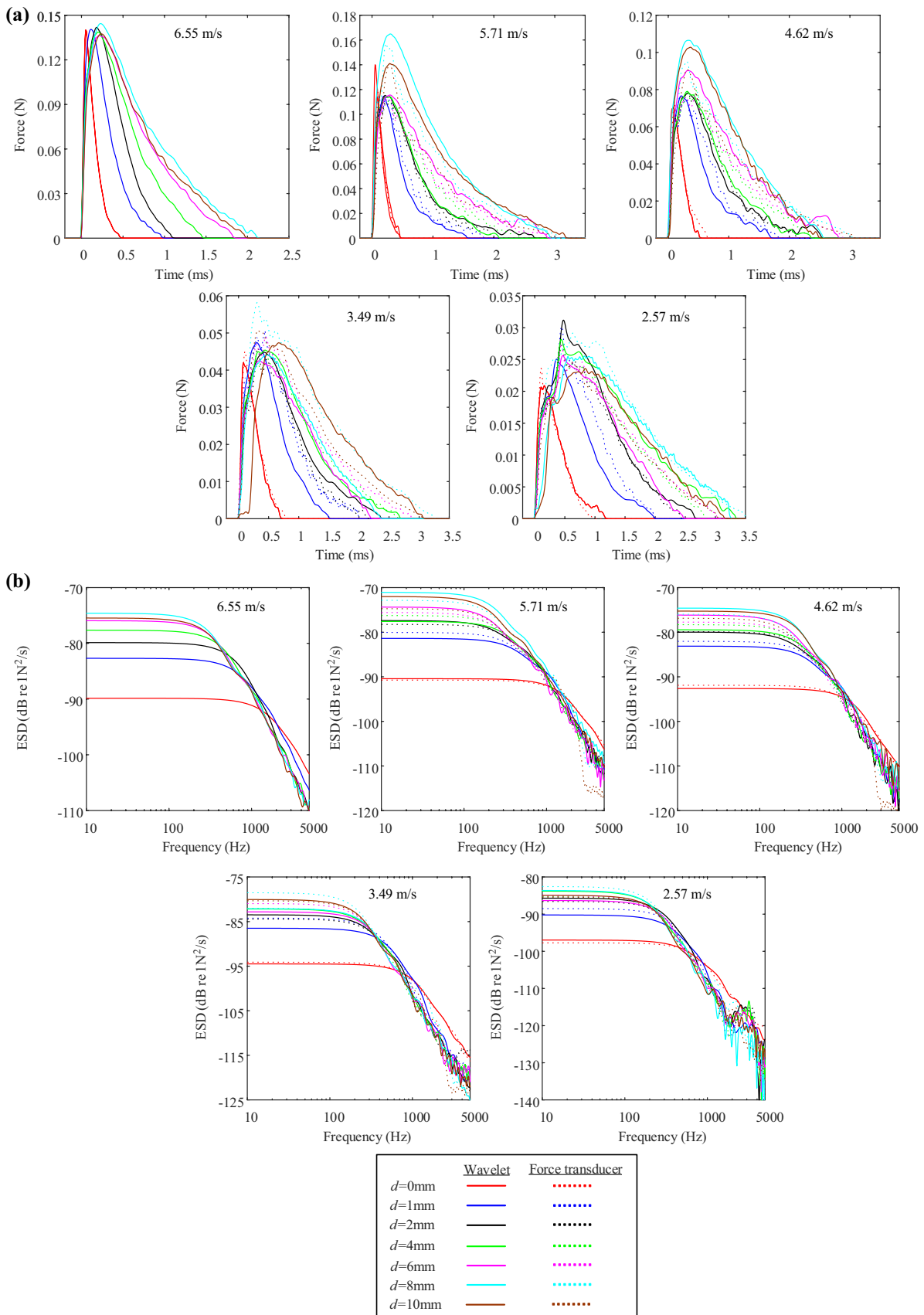### 4.4 Empirical formulae for the glass plate with and without a shallow water layer

In Sects. 4.2.2 and 4.2.3, empirical formulae were determined for 2 and 4.5 mm drops on dry glass for the full range of measured drop velocities. This section determines one set of empirical formulae with a practical application to rainfall where the drops impact at terminal velocity, and another set for lower drop velocities (between 2.57 and 5.71 m/s for 2 mm drops, and between 2.69 and 8.20 m/s for 4.5 mm drops). The advantage of this approach is that it is possible to minimise the errors for the practical application to rainfall at terminal velocity.

For 2 mm drops falling at terminal velocity onto a glass plate with or without a water layer, Eq. (26) is used with the empirical constants (C, α, and β) in Table 2.

deeper, the peak force decreases and the pulse width broadens. This results in higher forces at low-frequencies; for drops at terminal velocity this increase is up to ≈ 15 dB for 2 mm drops and ≈ 12 dB for 4.5 mm drops. Below terminal velocity the presence of a water layer also increases the force at low-frequencies; however, in the time domain the presence of a water layer can either increase or decrease the peak force. Petersson (1995) also noted that a water layer could increase the force at low-frequencies and attributed it to the energy of the drop being transferred to the water layer on the surface. However, this explanation does not seem sufficient to explain the differences in the peak force (time domain) with different drop velocities because it takes no account of the effect of drop velocity on coalescence with different water layer depths and the area over which the force is applied on the glass. At high frequencies there is evidence that, compared with dry glass, the water layer gives lower

For 4.5 mm drops falling at terminal velocity onto a glass plate with or without a water layer, the following equation is used:

$$
\begin{aligned}
F(t) = {} & C_1 \exp\left[-\frac{\left(\ln(1000t) + \alpha_1\right)^2}{\beta_1^{\,2}} \right] \\
& + C_2 \exp\left[-\frac{\left(\ln(1000t) + \alpha_2\right)^2}{\beta_2^{\,2}} \right],
\end{aligned} \tag{33}
$$

Fig. 11 Ratio of accelerance for a circle of in-phase force with radius, r, to point excitation **a** magnitude and **b** phase
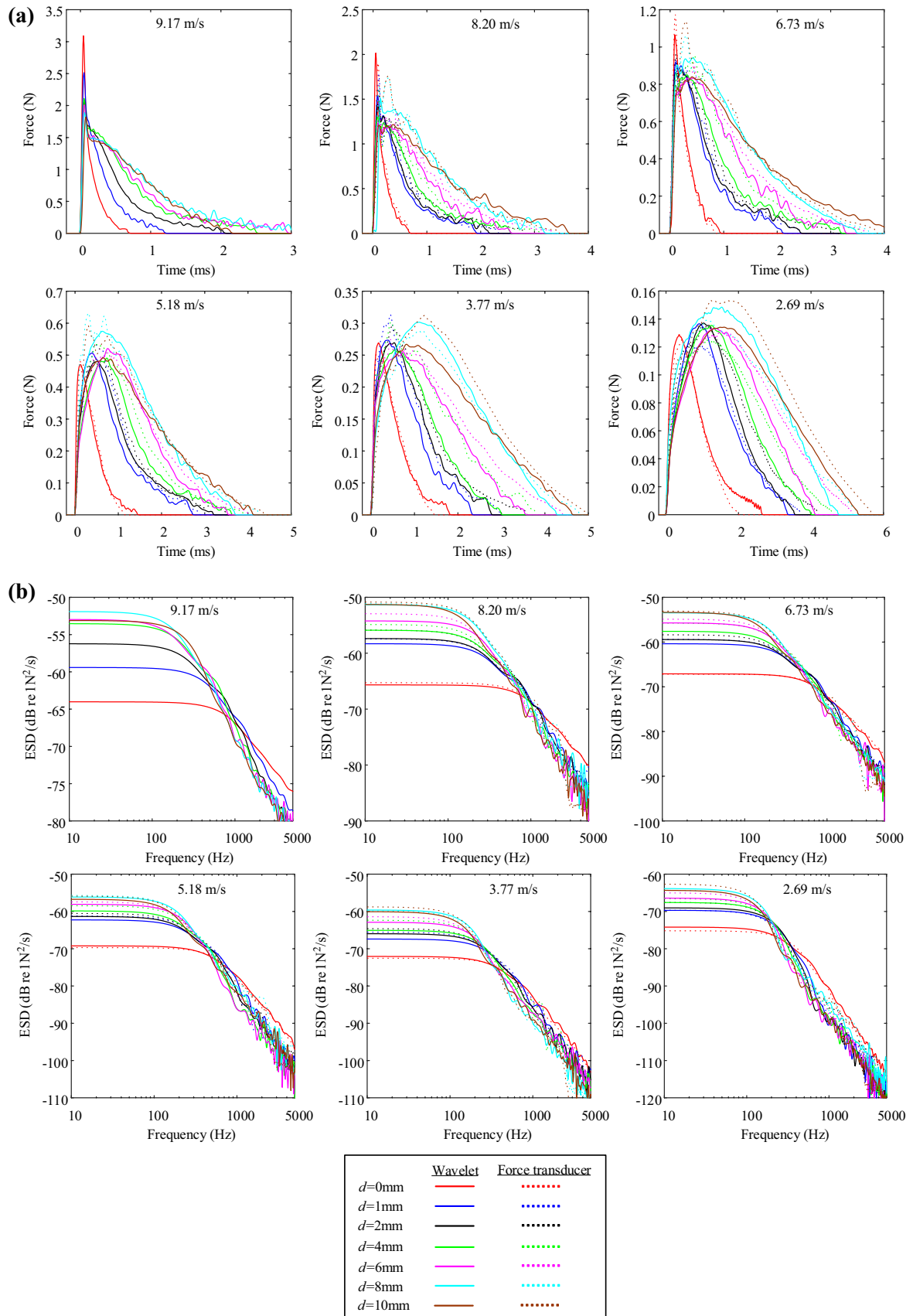
◀**Fig. 13** Measurements of initial impact force from 4.5 mm drops: **a** time-dependent force and **b** ESD with different drop velocities impacting the dry glass surface ($d=0$ mm) and different water layer depths on the glass from $d=1$ to 10 mm. Measurements use the wavelet approach (solid line) and force transducer (dotted line)

Table 2 Empirical formulae constants for 2 mm drops at terminal velocity

Water depth, d (mm)	C	α	β
0	0.1389	2.5912	0.9867
1	0.1504	2.0231	1.1196
2	0.1553	1.6889	1.1136
4	0.1504	1.5910	1.2567
6	0.1496	1.4639	1.3171
8	0.1534	1.4308	1.3934
10	0.1447	1.3864	1.3251

where the empirical constants C_i, α_i, β_i; $i=1$, 2 are given in Table 3.

For 2 and 4.5 mm drops falling at velocities lower than terminal velocity onto a glass plate with or without a water layer, the empirical constants (a_C, b_C, a_α, b_α, a_β, b_β) are given in Tables 4 and 5, respectively, to determine C, α and β as described by Eqs. (28, 29, 30).

For comparison with the empirical formulae, the time-dependent forces and the difference in the ESD values measured with the wavelet approach are shown on Figs. 14 and 15 for 2 and 4.5 mm drops respectively. At terminal velocity the empirical formulae for frequencies up to 1k Hz give an error < 0.5 dB for the dry surface (NB This is a lower error than was achieved with the empirical formula in Sect. 4.2.3) and < 2 dB for the shallow water layers. For drop velocities below terminal velocity, the error is typically < 5 dB below 1k Hz but this increases

Table 3 Empirical formulae constants for 4.5 mm drops at terminal velocity

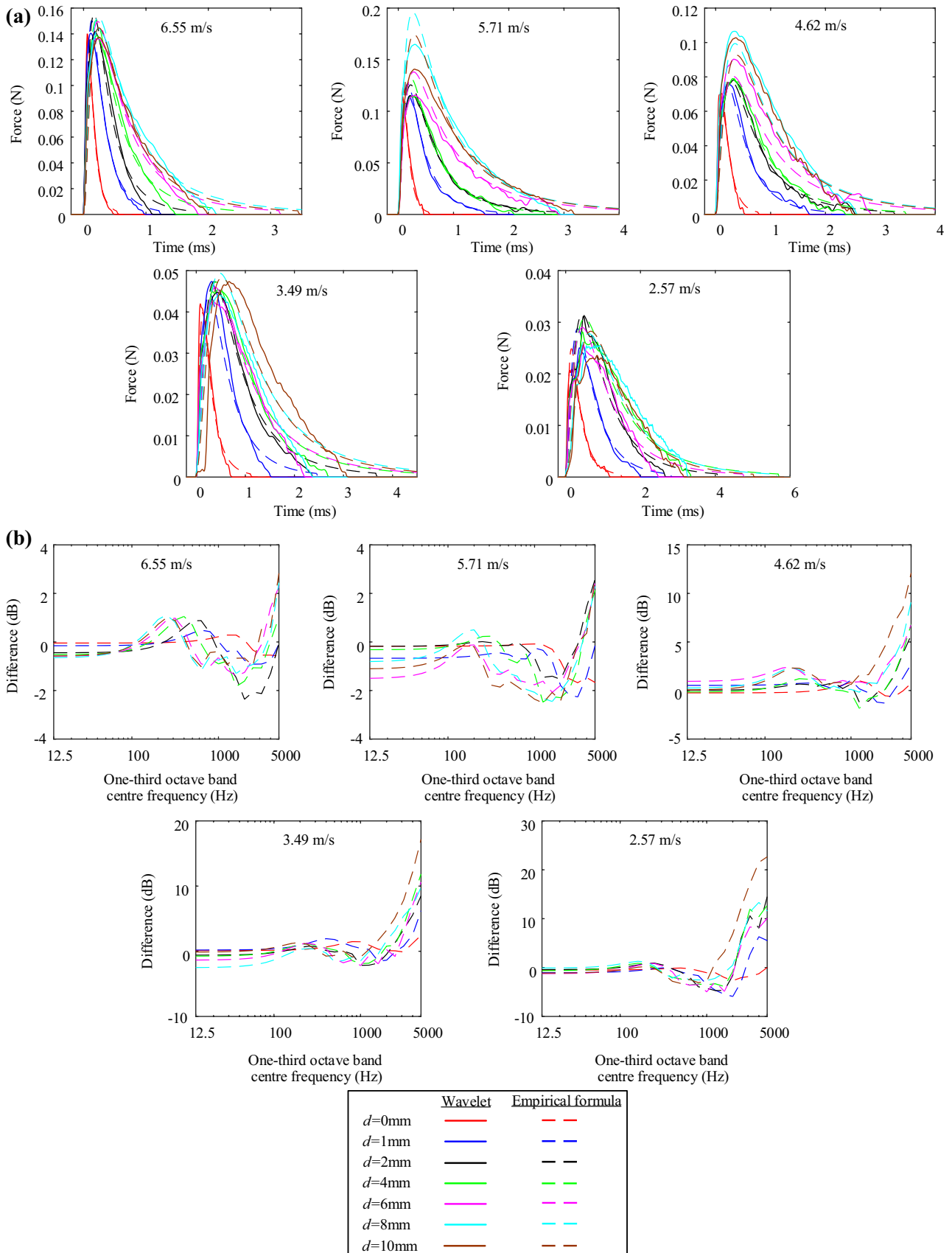| Water depth, d (mm)	C_1	C_2	α_1	α_2	β_1	β_2
0	2.7186	0	3.3367	0	1.5027	0
1	1.7168	1.5693	2.0703	2.8439	1.3129	0.4645
2	1.7673	1.2078	1.8683	2.8984	1.4361	0.509
4	1.7673	1.2220	1.6663	2.8479	1.5391	0.4787
6	1.7067	1.1250	1.5653	2.7873	1.5371	0.4403
8	1.6885	1.1008	1.4139	2.7408	1.5391	0.4726
10	1.6663	0.9756	1.3129	2.5934	1.3916	0.4141

Table 4 Empirical formulae constants for 2 mm drops at drop velocities that are lower than terminal velocity

Water depth, d (mm)	a_C	b_C	a_α	b_α	a_β	b_β
0	0.5088	−5.001	0.1748	1.3930	−0.0727	1.3148
1	0.4728	−4.7645	0.2003	0.5220	0.0270	0.9816
2	0.4402	−4.5871	0.2266	0.1213	0.0584	0.9180
4	0.4654	−4.6779	0.2605	−0.0738	0.0082	1.1615
6	0.4976	−4.8194	0.1749	0.2685	0.0918	0.9180
8	0.6225	−5.1825	0.2988	−0.3846	0.1187	0.7678
10	0.5801	−5.0568	0.3165	−0.5613	0.1493	0.5681

Table 5 Empirical formulae constants for 4.5 mm drops at drop velocities that are lower than terminal velocity

Water depth, d (mm)	a_C	b_C	a_α	b_α	a_β	b_β
0	0.4616	−3.1084	0.3391	0.2307	0.0381	1.1176
1	0.4227	−2.9358	0.3672	−0.7840	0.1314	0.5461
2	0.4153	−2.9193	0.3703	−0.9777	0.1392	0.4741
4	0.4035	−2.8740	0.3112	−0.9527	0.1106	0.5509
6	0.4011	−2.8439	0.2451	−0.7966	0.0654	0.8094
8	0.4023	−2.7031	0.2691	−0.9317	0.0796	0.8505
10	0.3947	−2.8019	0.2508	−0.8405	0.0875	0.8845

(a)

(b)

◀**Fig. 14** Initial impact force from 2 mm drops: comparison of measurements using the wavelet approach (solid line) and the empirical formula (dashed line) with different drop velocities impacting the dry glass surface ($d = 0$ mm) and different water layer depths on the glass from $d = 1$ to 10 mm. **a** Contains the time-dependent, zero-padded impact force and **b** contains the difference between the ESD from the wavelet measurement and the empirical formula in one-third octave bands

significantly at higher frequencies due to the empirical formula not accounting for ripples in the time domain that contain high-frequency energy.
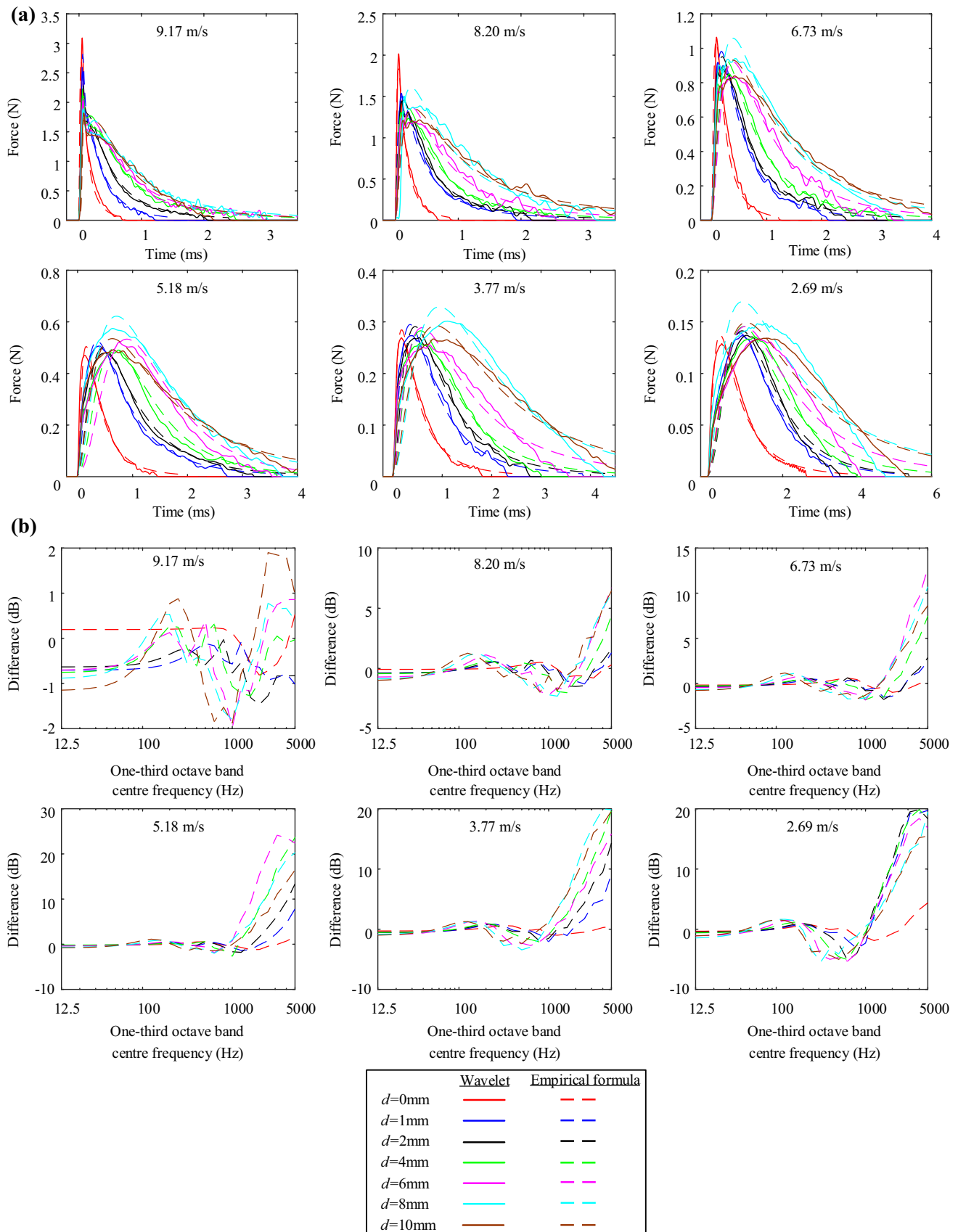
5 Conclusions

The impact force applied by 2 and 4.5 mm liquid water drops impacting an elastic plate with or without a still, shallow water layer at a range of drop velocities has been determined using wavelet deconvolution to overcome limitations of other measurement techniques. A wide range of fall heights has been used to estimate a new friction coefficient that can be used to calculate the drop velocity; this coefficient has wider applications to situations than previous work.

For drops on dry glass, the peak force increases and the pulse width of the impact force decreases with increasing drop velocity. Wavelet deconvolution was validated by its close agreement with force transducer measurements in the frequency domain. Paraboloidal, cylindrical–hemispherical, spherical, and ellipsoidal drop shape models underestimated the measured peak force at the highest velocities (including terminal velocity). Models from Roisman et al. and Marengo et al. underestimated the measured peak force at all velocities. The inability of all the prediction models to describe the peak force and the time-dependent force provided the motivation to develop empirical formulae.

For drops on a shallow water layer, high-speed camera images were used to identify distinct features relating to the splash that apply forces on the plate that occur after the initial impact, such as the crater, crown, and jet as well as bubble entrainment underneath the surface of the water. This leads to measurement problems when using a force transducer with a contained water layer because some features of the splash such as crater formation and outgoing capillary waves are no longer representative of the natural phenomena. Analysis of the measurement errors indicates that the wavelet approach can be used to estimate forces applied by the crater, crown, jet, vortex ring, or oscillating bubbles within 1 dB. However, there will be some low-level forces that cannot be accurately determined such as those from rebounding drops falling far from the original impact position, or capillary waves propagating away from the crater; fortunately their low-level makes them of little interest for the purpose of noise control. For 2 mm drops falling on 6, 8, and 10 mm layers, bubbles are regularly entrained in the water layer. Whilst the force from the initial impact tends to be significantly higher than the bubble-induced force below 200 Hz, the bubble-induced force above 700 Hz tends to become significantly higher than that from the initial impact with high peak levels at or above 6.5k Hz. Whilst these high forces from entrained bubbles are noteworthy, they are less critical when evaluating rain noise because (a) water layers on roof elements are typically < 6 mm deep and (b) the radiated sound only tends to be assessed at frequencies below 6.5k Hz.

Empirical formulae have been developed for 2 and 4.5 mm drops falling at (a) different velocities up to and including terminal velocity onto a dry glass surface, (b) terminal velocity onto dry glass or glass with a shallow water layer up to 10 mm and (c) different velocities below terminal velocity onto dry glass or glass with a shallow water layer up to 10 mm. This allowed the errors to be minimised for different applications. For drops on dry glass, the empirical formulae are only strictly applicable to a glass plate or a composite layered plate with a glass surface, although they apply to any other thickness of plate. All the empirical formulae can reasonably be applied to any plate material with a similar surface roughness and wettability.

(a)

9.17 m/s — Force (N) — Time (ms)

8.20 m/s — Force (N) — Time (ms)

6.73 m/s — Force (N) — Time (ms)

5.18 m/s — Force (N) — Time (ms)

3.77 m/s — Force (N) — Time (ms)

2.69 m/s — Force (N) — Time (ms)

(b)

9.17 m/s — Difference (dB) — One-third octave band centre frequency (Hz)

8.20 m/s — Difference (dB) — One-third octave band centre frequency (Hz)

6.73 m/s — Difference (dB) — One-third octave band centre frequency (Hz)

5.18 m/s — Difference (dB) — One-third octave band centre frequency (Hz)

3.77 m/s — Difference (dB) — One-third octave band centre frequency (Hz)

2.69 m/s — Difference (dB) — One-third octave band centre frequency (Hz)

Legend:

	Wavelet	Empirical formula
d=0mm		
d=1mm		
d=2mm		
d=4mm		
d=6mm		
d=8mm		
d=10mm		

◄**Fig. 15** Initial impact force from 4.5 mm drops: comparison of measurements using the wavelet approach (solid line) and the empirical formula (dashed line) with different drop velocities impacting the dry glass surface ($d=0$ mm) and different water layer depths on the glass from $d=1$ to 10 mm. **a** Contains the time-dependent, zero-padded impact force and **b** contains the difference between the ESD from the wavelet measurement and the empirical formula in one-third octave bands

References

Anantharamaiah N, Tafreshi HV, Pourdeyhimi B (2006) A study on hydroentangling waterjets and their impact forces. Exp Fluids 41(1):103

Ballagh KO (1990) Noise of simulated rainfall on roofs. Appl Acoust 31(4):245–264

Beard KV, Bringi VN, Thurai M (2010) A new understanding of raindrop shape. Atmos Res 97(4):396–415

Clift R, Grace JR, Weber ME (1978) Bubbles, drops, and particles. Academic Press, New York

Doyle JF (1997) A wavelet deconvolution method for impact force identification. Exp Mech 37(4):403–408

Fuchs NA (1964) The mechanics of aerosols. Pergamon Press, London

Grinspan AS, Gnanamoorthy R (2010) Impact force of low velocity liquid droplets measured using piezoelectric PVDF film. Colloids Surf A 356(1):162–168

Guigon R, Chaillout J-J, Jager T, Despesse G (2008) Harvesting raindrop energy: experimental study. Smart Mater Struct 17:015039

Hobbs PV, Osheroff T (1967) Splashing of drops on shallow liquids. Science 158(3805):1184–1186

Hopkins C (2012) Sound insulation. Routledge. ISBN: 978-0-7506-6526-1

IEC 60721-2-2:2013 Classification of environmental conditions—part 2-2: environmental conditions appearing in nature—precipitation and wind. International Electrotechnical Commission

IEC 721-2-2:1988 Classification of environmental conditions—Part 2-2: environmental conditions appearing in nature—precipitation and wind. International Electrotechnical Commission

Leighton TG (1994) The acoustic bubble. Academic Press, London, ISBN: 9780124124981

Li J, Zhang B, Guo P, Lv Q (2014) Impact force of a low speed water droplet colliding on a solid surface. J Appl Phys 116:214903

Macklin WC, Hobbs PV (1969) Subsurface phenomena and the splashing of drops on shallow liquids. Science 166(3901):107–108

Marengo M, Antonini C, Roisman IV, Tropea C (2011) Drop collisions with simple and complex surfaces. Curr Opin Colloid Interface Sci 16:292–302

Marshall JS, Palmer WMcK (1948) The distribution of raindrops with size. J Meteorol 5:165–166

Mitchell BR, Nassiri A, Locke MR, Klewicki JC, Korkolis YP, Kinsey BL (2016) Experimental and numerical framework for study of low velocity water droplet impact dynamics. In: ASME 2016 11th international manufacturing science and engineering conference. ASME

Nearing MA, Bradford JM (1987) Relationships between waterdrop properties and forces of impact. Soil Sci Soc Am J 51(2):425–430

Nearing MA, Bradford JM, Holtz RD (1986) Measurement of force vs. time relations for waterdrop impact. Soil Sci Soc Am J 50(6):1532–1536

Paige CC, Saunders MA (1982) LSQR: an algorithm for sparse linear equations and sparse least squares. ACM Trans Math Softw 8(1):43–71

Petersson BAT (1995) The liquid drop impact as a source of sound and vibration. Build Acoust 2:585–624

Prosperetti A, Oguz HN (1993) The impact of drops on liquid surfaces and the underwater noise of rain. Annu Rev Fluid Mech 25(1):577–602

Pumphrey HC, Elmore PA (1990) The entrainment of bubbles by drop impacts. J Fluid Mech 220:539–567

Range K, Feuillebois F (1998) Influence of surface roughness on liquid drop impact. J Colloid Interface Sci 203(1):16–30

Rioboo R, Marengo M, Tropea C (2002) Time evolution of liquid drop impact onto solid, dry surfaces. Exp Fluids 33:112–124

Rodriguez F, Mesler R (1985) Some drops don't splash. J Colloid Interface Sci 106(2):347–352

Roisman IV, Romain R, Tropea C (2002) Normal impact of a liquid drop on a dry surface: model for spreading and receding. Proc R Soc Lond Ser A 458:1411–1430

Roisman IV, Berberović E, Tropea C (2009) Inertia dominated drop collisions. I. On the universal flow in the lamella. Phys Fluids 21:052103

Roux DCD, Cooper-White JJ (2004) Dynamics of water spreading on a glass surface. J Colloid Interface Sci 277(2):424–436

Soto D, De Lariviere AB, Boutillon X, Clanet C, Quéré D (2014) The force of impacting rain. Soft Matter 10(27):4929–4934

Suga H, Tachibana H (1994) Sound radiation characteristics of lightweight roof constructions excited by rain. Build Acoust 1(4):249–270

Vaseghi SV (2013) Bayesian estimation, Chap. 4. In: Vaseghi SV (ed) Advanced signal processing and digital noise reduction, 2nd edn. Springer. ISBN: 0-471-62692-9

Zhang B, Li J, Guo P, Lv Q (2017) Experimental studies on the effect of Reynolds and Weber numbers on the impact forces of low-speed droplets colliding with a solid surface. Exp Fluids 58(9):125